Effect of unsaturated flow modes on partitioning dynamics of gravity-driven flow at a simple fracture intersection: Laboratory study and three-dimensional smoothed particle hydrodynamics simulations

Jannes Kordilla[1], **Torsten Noffz**[1], **Marco Dentz**[2], **Tobias Geyer**[3], **Alexandre M. Tartakovsky**[4]

[1]University of Göttingen, Geoscientific Centre, Göttingen, Germany

[2]Institute of Environmental Assessment and Water Research (IDAEA), Spanish National Research Council (CSIC), Barcelona, Spain

[3]Regierungspräsidium Freiburg, Landesamt für Geologie, Rohstoffe und Bergbau, Freiburg, Germany

[4]Pacific Northwest National Laboratory, Computational Mathematics Group, Richland, Washington USA

Key Points:

- = partitioning dynamics at wide aperture fracture intersections depend on unsaturated flow modes
- = onset of characteristic Washburn regime from non-equilibrium conditions until steady state is determined
- = smoothed particle hydrodynamics can reproduce complex free surface flows dominated by surface tension

Corresponding author: Jannes Kordilla, jkordil@gwdg.de

Abstract

In this work, we study gravity-driven flow of water in the presence of air on a synthetic surface intersected by a horizontal fracture and investigate the importance of droplet and rivulet flow modes on the partitioning behavior at the fracture intersection. We present laboratory experiments, three-dimensional smoothed particle hydrodynamics (SPH) simulations using a heavily parallelized code, and a theoretical analysis. The flow-rate-dependent mode switching from droplets to rivulets is observed in experiments and reproduced by the SPH model, and the transition ranges agree in SPH simulations and laboratory experiments. We show that flow modes heavily influence the "bypass" behavior of water flowing along a fracture junction. Flows favoring the formation of droplets exhibit a much stronger bypass capacity compared to rivulet flows, where nearly the whole fluid mass is initially stored within the horizontal fracture. The effect of fluid buffering within the horizontal fracture is presented in terms of dimensionless fracture inflow so that characteristic scaling regimes can be recovered. For both cases (rivulets and droplets), the flow within the horizontal fracture transitions into a Washburn regime until a critical threshold is reached and the bypass efficiency increases. For rivulet flows, the initial filling of the horizontal fracture is described by classical plug flow. Meanwhile, for droplet flows, a size-dependent partitioning behavior is observed, and the filling of the fracture takes longer. For the case of rivulet flow, we provide an analytical solution that demonstrates the existence of classical Washburn flow within the horizontal fracture.

1 Introduction

In unsaturated rocks, gravity-driven flow on fracture walls and in fracture networks can lead to the formation of vertical preferential flow paths [*Nimmo*, 2012; *Faybishenko et al.*, 2015]. Along such flow paths, intersections with sub-vertical fractures form critical relay points, which control the partitioning behavior into the adjacent fracture(s) [*Wood et al.*, 2002; *LaViolette*, 2003; *Ji et al.*, 2006; *Nicholl and Glass*, 2005]. Depending on the geometry, intersections may act as temporary capillary barriers and induce pulsating flows. This has been shown for orthogonal quasi two-dimensional fracture networks with slightly irregular geometry [*Glass et al.*, 2003], and well-controlled orthogonal cross sections with perturbations of the geometry (vertical and horizontal offsets, detritus at the intersection center) [*Wood et al.*, 2005]. The authors found that for most flow rates a capillary barrier is established at the intersection, which channels water into the the perpendicular fractures.

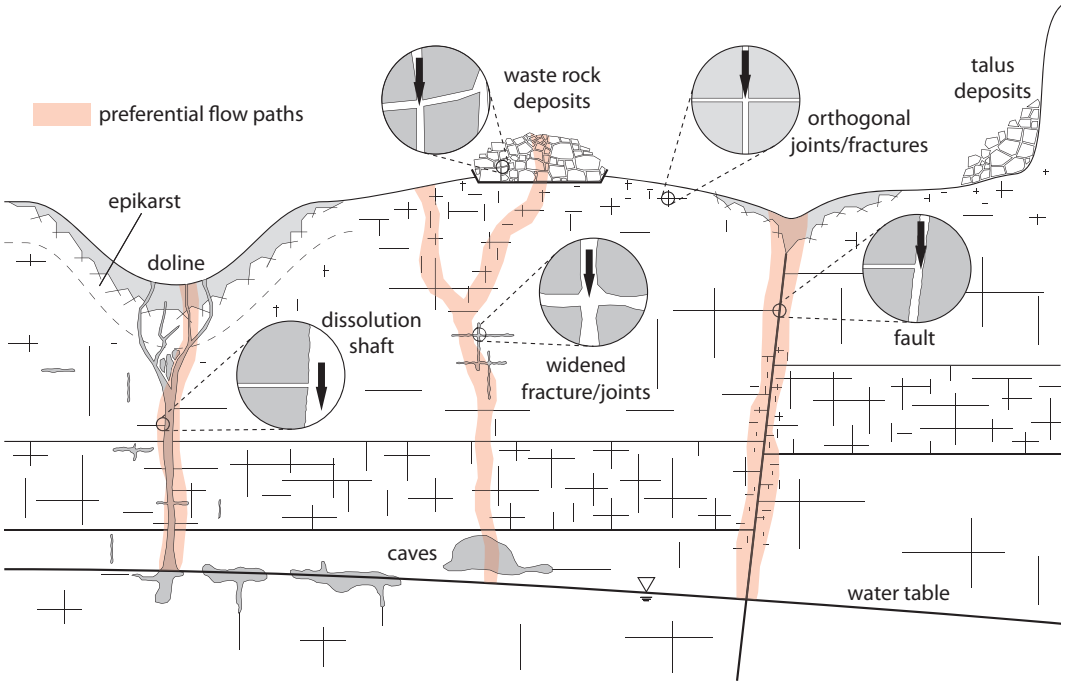

Figure 1. Conceptual model for the occurrence of preferential unsaturated flow in fractured media with a focus on wide aperture vertical flow paths intersected by sub-vertical fractures. Based on concepts for recharge through dissolution shafts in karst systems [*Gunn*, 1981; *Williams*, 2008], unsaturated flow in widened fractures [*Dahan et al.*, 1999, 2000], flow through talus and leaching of waste rock deposits [*Tokunaga et al.*, 2005; *Trinchero et al.*, 2011], rapid vertical recharge through fault zones [*Bodvarsson et al.*, 1997; *Liu et al.*, 2004], and simplified orthogonal structure of fracture systems [*Barenblatt et al.*, 1960; *Dershowitz and Einstein*, 1988; *Guarracino*, 2006].

The capillary barrier is breached once the water height in the vertical fracture above the intersection reaches a critical value, and water is then released into the vertical fracture below the intersection. At higher flow rates a continuous rivulet (or tendril) between upper and lower vertical fracture is established and a steady flow regime can be observed.

The accumulation and release of water results in pulsating flows with magnitudes of temporal outflow fluctuations much higher than dripping dynamics in individual fractures alone can explain [*Su et al.*, 1999], highlighting the importance of fracture intersections (specifically the sub-vertical fractures) as potential storage zones. Furthermore, the partitioning process at fracture intersections leads to flow focussing or splitting [*Wood et al.*, 2005; *Wood and Huang*, 2015], which essentially controls the lateral and vertical dispersion characteristics of preferential flow paths (zones) [*Glass and LaViolette*, 2004]. Hence, the analysis of flow partitioning at fracture intersections can ultimately lead to the interpretation and understanding of large-scale vertical flow structures. While intersections can act as flow integrators and, therefore, lead to large-scale convergence with increasing depth, they can also work against convergence due to flow path splitting.

Previous research in this field has mainly focussed on rather small aperture fractures ranging from sub-millimeter size [*Glass et al.*, 2003; *Ji et al.*, 2004, 2006; *Nicholl and Glass*, 2005] dominated by capillary forces, over scales around 0.7 mm at the capillary-inertial transition [*Wood et al.*, 2002, 2005], and larger apertures or free fracture surfaces within the inertial-dominated regime [*Tokunaga and Wan*, 1997, 2001; *Dragila and Weisbrod*, 2004; *Tartakovsky and Meakin*, 2005a; *Huang et al.*, 2005; *Liu et al.*, 2007]. Field evidence suggests the existence of wide fractures with apertures of several millimeters in many geological systems (see Fig. 1 and references therein). In contrast, flows in vertical wide aperture fractures are not bounded by a second surface and dominated by gravitational forces, which gives rise to various flow modes ranging from droplets, over rivulets to (wavy) films with increasing flow rates [*Ghezzehei*, 2004; *Dragila and Weisbrod*, 2003].

While for small aperture fractures, specifically with orthogonal geometry, capillary barriers and flow pulsation are the dominating processes, for wide aperture systems sub-vertical fractures provide a storage, which may not trigger flow fluctuation. Instead water is metered into the sub-vertical fracture until flow converges into a steady-state, and outflow fluctuations are entirely due to the flow fragmentation on the vertical surface (snapping droplets, rivulets). As demonstrated in this work, the partitioning at the fracture in-

tersection is strongly dominated by flow modes. Despite the efforts made by previous researchers to understand the mechanistic details of the partitioning and the bulk behavior for small aperture systems mainly in terms of geometry, to the best of our knowledge, the relation between unsaturated gravity-driven flow mode and the dynamics of flow partitioning have not yet been demonstrated for wide aperture systems and longer time scales.

Numerical models for this specific class of fluid flow problems have to resolve various processes, including the complex evolution of fluid-air interfaces, formation of singularities (e.g., droplet breakups), flow mode switching, and dynamic contact angles. Lagrangian methods, such as smoothed particle hydrodynamics (SPH), provide a meshfree discretization of the Navier-Stokes equations. Other Lagrangian methods, including dissipative particle dynamics (DPD) [*Hoogerbrugge and Koelman*, 1992] and molecular dynamics (MD) [*Alder and Wainwright*, 1959], also have been used to model fluid flow. Unlike mesoscale (DPD) and microscale (MD) methods, SPH is a "macroscopic" method. Due to the Lagrangian framework properties, SPH has several advantages, specifically in the case of free surface flow dynamics, i.e., for simulation domains that are only sparsely populated with a fluid phase. For example, momentum, mass, and energy are explicitly conserved [*Monaghan*, 1982]; multiphase interfaces are clearly represented by individual particles and do not require front-tracking algorithms [*Wang et al.*, 2016]; free surfaces (fluid-gas interfaces) can be easily modeled, saving computational resources [*Sigalotti et al.*, 2006]; physical phenomena, such as surface tension and contact angle, naturally arise from pairwise particle interactions [*Tartakovsky and Meakin*, 2005a; *Kordilla et al.*, 2013; *Tartakovsky and Panchenko*, 2016]; and the non-linear advection term is absent in the Lagrangian method for the momentum conservation equation [*Monaghan*, 2005].

This work focuses on the specific case of flow along a vertical free surface, connected to a horizontal wide aperture fracture (2.5 mm). As we do not consider exchange with the porous matrix, redistribution or partitioning under dynamic flow conditions can only occur within a connected fracture element. According to the previously introduced force balance estimates, free surface flow in the vertical fracture is dominated by the gravitational forces, leading to the formation of droplets and rivulets. In contrast, in the horizontal fractures, the capillary forces are expected to dominate. To our knowledge, this is the first experimental and numerical investigation of flow in a vertical fracture intersected by a horizontal fracture at timescales sufficiently long to study the travel time distribution. The main objective of this work is to identify parameters that affect flow partitioning dy-

namics of such flows. The Reynolds numbers (Re) in our experiments are in the upper range of Re usually observed in the field. Therefore, the observed travel times correspond to the the lowermost spectrum of the travel time distribution. For constant inflow conditions, the effect of flow mode formation on the non-equilibrium volumetric outflow rate is numerically studied with both a new massively parallel three-dimensional SPH code and laboratory experiments that serve as a validation for our new SPH code. The efficiency of horizontal fracture imbibition, i.e., the bypass behavior, is shown to depend on the type of flow mode that prevails on the vertical fracture surface. Furthermore, our setup permits investigating the effect of a horizontal fracture, which takes the role of a storage component, until steady-state flow is reached. We also provide an analytical solution and demonstrate the temporary existence of characteristic plug flow and Washburn-type flow [*Bell and Cameron*, 1906; *Washburn*, 1921] regimes.

2 Methods

2.1 Laboratory setup

Here we describe our laboratory setup for the two main experiments, carried out to study the partitioning behavior of flow along a vertical surface intersected by a horizontal fracture. Parts of the setup are used for the validation studies as well. Details of the laboratory equipment and materials are provided and the general experimental setup is illustrated in Figure 2.

2.1.1 Single-inlet partitioning dynamics

With the first experiment we investigate the process of fractionation for a single tube inlet and cubes separated by a distance spacer with a thickness of $d_f = 2.5\,\mathrm{mm}$. At this spacing, the fractionation process at the intersection between horizontal fracture and vertical surface is controlled by a complex interplay of inertia and capillary forces, i.e., the prevailing flow mode. Distilled water is injected at the top of the upper cube (shown in Fig. 2), such that an immediate capillary connection is established. Flow rates are varied in the range of 1.5–4.5 $\mathrm{mL\,min^{-1}}$ at an interval of 0.1 $\mathrm{mL\,min^{-1}}$. Each experiment is run for 90 s, and the ratio of injected to total water mass leaving the system is recorded. We carry out 10 experiments at each flow rate and obtain the ensemble average.

2.1.2 Multi-inlet partitioning dynamics

For the second experiment the previous single-inlet experiments are extended to increase the number of injection points. Two different fluid injection schemes are chosen, so the resulting flow modes are either mainly in the droplet or rivulet regime. This allows us to examine the short and long timescale partitioning dynamics until steady state is reached (i.e., the horizontal fracture is completely filled) and to reduce the variance in outcomes because of the higher number of streams per experiment (a higher number of inlets helps to homogenize the influence of erratic droplet flow velocities within each inlet stream path).

In the first injection scheme, the laboratory setup consists of 15 injection points (here referred to as "point-wise" or "localized injection") equally distributed along the top of the upper cube with a total flow rate of 37.5 mL min^{-1}, i.e., the dominating flow mode within each flow path is droplet flow (see Fig. 9, left). The cubes are separated by a distance of 2.5 mm. During the experiments, the accumulated fluid mass that reaches the bottom of the system is measured using the digital scale. The second injection scheme is created by reducing the number of injection points to six and keeping the same total flow rate. This scheme enforces the formation of rivulets along each flow path.

2.1.3 Laboratory equipment and materials

For the percolation experiment, we use a 24-channel laboratory dispenser (Ismatec® IPC High Precision Multichannel Dispenser ISM934C), which has a flow rate precision of 0.1 %. The model consists of a planetary drive with automatic occlusion cartridges and provides flow rates ranging from 0.002 ml/min at 0.4 rpm to 44 ml/min at 45 rpm. As the rotation frequency is well below the frequency of droplet formation, effects of pump pulsation are unlikely to occur. The absolute flow rate is calibrated by an internal pump calibration system before each experiment. In addition, we conducted a mass balance study using a digital scale to check if flow rates are properly maintained over a longer time period.

Silicone tube inlets have an outer diameter of $\varnothing_{o1} = 3.5$ mm (inner diameter of $\varnothing_{i1} = 1.5$ mm) and are attached to an acrylic glass plate via drill holes. PTFA (Teflon®) tubes with an outer diameter of $\varnothing_{o2} = 1.59$ mm (inner diameter of $\varnothing_{i2} = 1.0$ mm) are inserted into the silicone tubes. The top plate is placed onto the upper cubes and slightly

offset to allow controlled placement of the PTFA injection tubes evenly distributed across the width of the cube. Injection tubes are put into direct contact with the vertical cube surfaces to allow immediate capillary contact with the surface.

The cubes have dimensions of $20 \times 20 \times 20$ cm and are made of clear poly(methyl methacrylat) (PMMA). Static contact angles θ_0 of the surfaces are 65.16°(±2.91°) and were experimentally determined with a contact angle goniometer. Sessile droplets have an average volume of 1.74 µL (±0.12 µL). The cubes are custom made with five sides glued to the miter, while one side is glued to the butt joint. Corners are polished and blurred on all sides, which creates a corner chamfer of 45° with an average length of 0.4 mm (see inset of Fig. 2). It should be noted that corners with a chamfer size of less then about 0.2 mm are used for the experiments. As this is close to the resolution of our simulations, the corner chamfers have not been explicitly resolved but are kept at a strict right angle. The surface flatness is measured with a dial gauge. Deviations from a reference height (taken to be the center of each cube) are taken at 25 positions (5×5 grid) on each surface of the cubes and three different cubes. The average deviation from the reference plane is 53.7 µm, and the averaged standard deviation is 19.2 µm.

Cubes are stacked on top of each other and separated by four metallic distance spacers with varying thickness d_f and a diameter of 5 mm. The base of the experimental setup consists of a metallic square grill with cell sizes of $5 \times 5 \times 5$ cm and is coated with a hydrophobic lacquer ($\theta_0 \approx 110°$) to maximize flow velocities across the grill. The drip water is collected by a digital scale beneath the grill within an accuracy of 0.01 ml. The additional travel time from the bottom of the cubes into the drip collector was experimentally determined to be below 500 ms and does not significantly influence the overall results.

Evaporation rates from the collector pan were determined for a constant room temperature and are accounted for during the experiments. The room is connected to a laboratory air conditioning system with a constant room temperature of 19 °C. We measured the evaporation rate from the digital scale before every experiment by adding a small amount of water onto its surface. Considering that each experimental run takes less than about 2 min, we corrected the measured mass by this rate. It should be noted that the total evaporated mass accounts for less than about 0.1 % of the total injected mass for each experimental run.

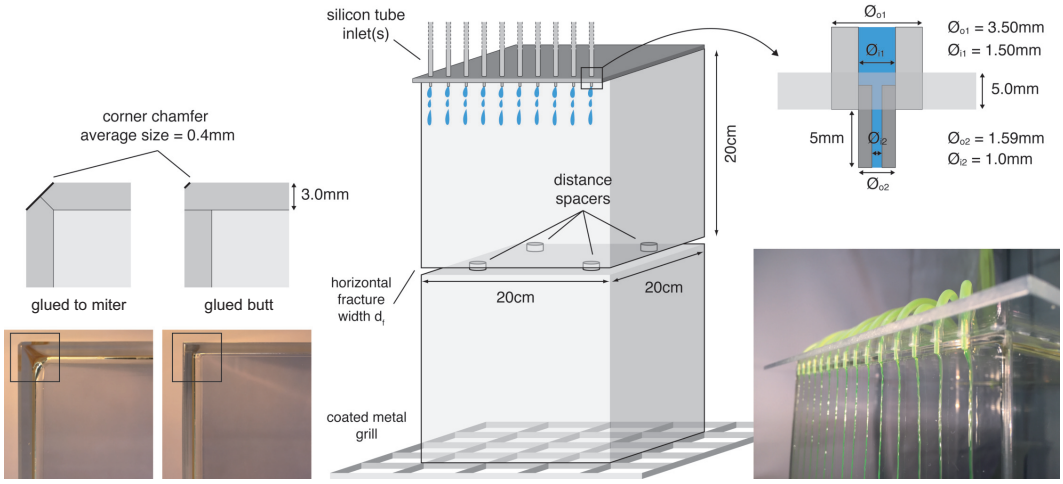

Figure 2. Laboratory setup and details of the fluid injection setup (right) and the custom-made cubes (left).

We use distilled water for all experiments. However, fluorescent dye (uranine) was added to increase visibility in some of the figures.

2.2 Numerical Smoothed Particle Hydrodynamics model

To numerically study the given system, we employ a massively parallel SPH code implemented within the LAMMPS (Large-scale atomic/molecular massively parallel simulator [*Plimpton*, 1995; *Plimpton et al.*, 2007; *Ganzenmüller et al.*, 2011]) framework. In its original form, LAMMPS has been developed for MD simulations. However, because of the similarities between the form of SPH and MD equations (e.g., particle-based flow field, link-lists, nearest neighbor search), many features of LAMMPS are also beneficial for the SPH implementation in a numerical code. This includes a domain-based decomposition of the particle field for efficient message passing interface (MPI) parallelization and an adaptive processor allocation, i.e., dynamic load balancing. Specifically, the latter feature becomes important when simulations consist of sparsely populated domains (e.g., in the case of free surface fracture flows) to optimize the per-processor particle load. In the following, we briefly describe our SPH model. In-depth reviews of the SPH method and its various flavors can be found, for example, in *Monaghan* [1992, 2005], *Liu and Liu* [2000, 2010], and *Tartakovsky et al.* [2016].

2.2.1 Governing equations

Free surface flow of water in a fracture can be described by the Navier-Stokes (linear momentum conservation) equations combining the momentum conservation equation:

$$\frac{d\mathbf{v}}{dt} = -\frac{\nabla P}{\rho} + \frac{\mu}{\rho}\nabla^2\mathbf{v} + \mathbf{g} \tag{1}$$

and the continuity equation

$$\nabla \cdot \mathbf{v} = 0, \tag{2}$$

subject to the no-slip boundary condition at the fluid-solid interface, Young boundary condition at the fluid-air-solid interface, and Young-Laplace boundary condition at the fluid-gas (water-air) interface [*Tartakovsky and Panchenko*, 2016]. Here, $\mathbf{v}$ is the fluid velocity, P is the pressure, μ is the viscosity, ρ is the density, and $\mathbf{g}$ is the gravitational acceleration.

2.2.2 Overview of the SPH method

In SPH, a continuous field, e.g., a fluid, is generally discretized with nonuniformly distributed "particles." The term "particle" does not imply a specific shape (i.e., a spherical shape), but it must be understood in the sense of a mathematical integration point. Despite this important distinction, particles are associated with a volume and constant mass. The particle volume is constant or changes depending on flow being incompressible or compressible.

The SPH approximation of a field variable (e.g., density and velocity) relies on the following fundamental integral representation of a continuous field defined over the domain Ω:

$$F(\mathbf{r}) = \int_\Omega F(\mathbf{r}')\delta(\mathbf{r} - \mathbf{r}')d\mathbf{r}', \tag{3}$$

where F is a field variable, $\mathbf{r}$ is the position vector, and δ is the Dirac delta function. It is apparent that an approximation to this formulation is required in a numerical context, which is given by

$$\langle F(\mathbf{r})\rangle = \int_\Omega F(\mathbf{r}')W(|\mathbf{r} - \mathbf{r}'|, h)d\mathbf{r}', \tag{4}$$

where W is the so-called "interpolation kernel" or "smoothing function" that establishes a weighted contribution of $F(\mathbf{r}')$ to $\langle F(\mathbf{r})\rangle$ within the support range h from r. The kernel function satisfies the following properties: (1) it has the compact support h, that is

$$W(|\mathbf{r} - \mathbf{r}'|, h) = 0 \qquad \text{for} \qquad |\mathbf{r} - \mathbf{r}'| > h, \tag{5}$$

(2) it satisfies the unity condition

$$\int_{\Omega} W(|\mathbf{r}-\mathbf{r}'|,h)dr' = 1, \tag{6}$$

and (3) the Dirac delta function behavior can be recovered as

$$\lim_{h\to 0} W(|\mathbf{r}-\mathbf{r}'|,h) = \delta(\mathbf{r}-\mathbf{r}')\,. \tag{7}$$

The shape of the kernel function commonly resembles a Gaussian function. In this work, we employ the so-called "Wendland kernel" [*Wendland*, 1995]:

$$W(q,h) = \alpha_k \begin{cases} (1-q)^3 & 0 \le q < 1 \\ 0 & 1 \le q\,, \end{cases} \tag{8}$$

where $r = |\mathbf{r}-\mathbf{r}'|$, $q = r/h$, and $\alpha_k = 168/(16\pi h^3)$. The Wendland kernel has been shown to have better stability properties than spline function kernels [*Dehnen and Aly*, 2012], which are another popular choice in SPH simulations.

Equation (4) can be casted into a discrete summation form to obtain the general field approximation for a field value at point i:

$$\langle\langle F_i \rangle\rangle = \sum_{j=1}^{N} \frac{m_j}{\rho_j} F_j W(|\mathbf{r}_i - \mathbf{r}_j|, h), \tag{9}$$

where m_j is the mass, ρ_j is the particle density, and N is the total number of particles that discretize the domain. Similarly, the gradient of a field value can be easily approximated by differentiation of the kernel instead of the function itself so

$$\langle\langle \nabla F_i \rangle\rangle = \sum_{j=1}^{N} \frac{m_j}{\rho_j} F_j \nabla W(|\mathbf{r}_i - \mathbf{r}_j|, h)\,. \tag{10}$$

For simplicity, we drop the double approximation brackets in the following and adopt the notation $\vec{\square}_i - \vec{\square}_j = \vec{\square}_{ij}$ and $|\vec{\square}_i - \vec{\square}_j| = \square_{ij}$.

The SPH particle approximation of fields and spatial derivatives, Eqs. (9) and (10), are used to discretize the Navier-Stokes equations. In this work, we use the pairwise force-SPH (PF-SPH) method to impose the Young-Laplace and Young boundary conditions [*Tartakovsky and Panchenko*, 2016; *Kordilla et al.*, 2013]:

$$m_i \frac{d\mathbf{v}_i}{dt} = \sum_{j=1}^{N} F_{ij}^P + \sum_{j=1}^{N} F_{ij}^V + \sum_{j=1}^{N} F_{ij}^I + F_i^g\,, \tag{11}$$

where F_{ij}^P is the force between particles i and j resulting from the pressure gradient discretization, F_{ij}^V is a viscous force arising from the viscous term discretization, and F_i^g is

a body force acting on particle i. In this approach, the solid phase (i.e., the fracture wall) is discretized with "solid" particles placed uniformly within distance h from the fluid-solid interface. The solid particles are assigned zero velocity, while the density and viscosity of water are included in the summations in Eq. (11). The conservative interaction force F_{ij}^I is different for interactions between two fluid particles and fluid and solid particles. In the following, we describe these components and the additional equations required to time integrate the SPH discretization of the Navier-Stokes equation.

2.2.3 Equation of state

Incompressible flow equations can be solved with SPH using the projection method [*Hu and Adams*, 2007; *Cummins and Rudman*, 1999]. To avoid solving the associated Poisson equation for pressure, here we use a weakly compressible SPH scheme that approximates an incompressible fluid as a compressible fluid. To do so, we replace Eq. (2) with

$$\frac{d\rho}{dt} = -\rho \nabla \cdot \mathbf{v}, \tag{12}$$

and close Eqs. (1) and (12) with the equation of state [*Monaghan*, 2005; *Batchelor*, 2000]:

$$P(\rho) = c_0^2 \frac{\rho_0}{7} \left(\left[\frac{\rho}{\rho_0} \right]^7 - 1 \right) + P_0, \tag{13}$$

where ρ_0 is the reference water density and P_0 is a background pressure. The speed of sound c_0 is problem dependent and is chosen so that the fluid behaves nearly incompressible. The ratio $|\delta\rho|/\rho \leq 0.03$, where $|\delta\rho|$ is the maximum absolute change in density, has proven to be sufficient to model accurate pressure fields [*Morris et al.*, 1997].

2.2.4 Mass conservation

The density ρ_i can be found via an SPH discretization of the continuity (mass conservation) equation, Eq. (12), and the general field approximation, Eq. (9),

$$\frac{d\rho_i}{dt} = \sum_{j=1}^{N} m_j \mathbf{v}_{ij} \cdot \hat{\mathbf{e}}_{ij} \frac{\partial W(\mathbf{r}_{ij}, h)}{\partial r_{ij}}, \tag{14}$$

where $\hat{\mathbf{e}}_{ij} = \mathbf{r}_{ij}/r_{ij}$ is the unit vector pointing from particle i to particle j. In this work, we use a "kernel summation" instead

$$\rho_i = \sum_{j=1}^{N} m_j W(\mathbf{r}_{ij}, h), \tag{15}$$

to obtain the mass density at each time step. The former option is computationally more efficient as the density can be obtained simultaneously with the velocity calculations. However, it is known to not exactly conserve mass and requires occasional correction steps of the particle densities using Eq. (15) [*Monaghan*, 2005]. Furthermore, it has not yet been shown to produce stable free surface flow dynamics, including the effect of surface tension.

2.2.5 Pressure gradient

The pressure gradient is commonly casted into a symmetric form [*Monaghan*, 1982, 1992]

$$F_{ij}^{P} = m_i \left(\frac{1}{\rho} \nabla P \right)_i = \sum_{j=1}^{N} m_i m_j \left(\frac{P_i}{\rho_i^2} + \frac{P_j}{\rho_j^2} \right) \hat{\mathbf{e}}_{ij} \frac{\partial W(\mathbf{r}_{ij}, h)}{\partial r_{ij}} \,. \tag{16}$$

Due to its symmetric form, the preceding discretization conserves momentum exactly.

2.2.6 Viscosity

The Laplacian in Eq. (1) can theoretically be directly solved by looping twice over the particle field [*Watkins et al.*, 1996]. However, as this approach requires about twice the computational effort, various alternative approximations have been derived [*Monaghan*, 2005; *Cleary*, 1998]. In this work, we use the form of *Morris et al.* [1997]

$$F_{ij}^{V} = m_i \left(\frac{\mu}{\rho} \nabla^2 \mathbf{v} \right)_i = \sum_{j=1}^{N} m_i m_j \frac{\mu_i + \mu_j}{\rho_i \rho_j} \frac{\mathbf{v}_{ij}}{r_{ij}} \frac{\partial W(\mathbf{r}_{ij}, h)}{\partial r_{ij}} \,, \tag{17}$$

which has been demonstrated to exactly conserve linear momentum.

2.2.7 Boundary conditions

In SPH, the no-slip boundary condition at the fluid-solid boundary can be imposed by using ghost particles that mirror fluid particles in the direction normal to the nominal solid interface [*Libersky et al.*, 1993] or uniformly distributed in the solid phase (i.e., the fracture wall) [*Morris et al.*, 1997; *Zhu et al.*, 1999]. These methods require determining the ratio of normal distances from fluid and mirror particles to the nominal solid boundary (the proximity ratio), which becomes challenging for highly irregular surfaces. Moreover, the computational costs of these methods are high compared to simpler bounce-back conditions, as demonstrated by *Tartakovsky and Meakin* [2006], *Tartakovsky et al.* [2009] and *Kordilla et al.* [2013]. In this work, we use the method of *Morris et al.* [1997] com-

bined with the proximity ratio determination of *Holmes et al.* [2011]. To approximate the nominal solid-fluid boundary within the diffuse interface region of an irregular surface, a state-specific number density is employed:

$$n^s_{i,\alpha} = \sum \delta_{\alpha,\beta} W(\mathbf{r}_{i,\alpha} - \mathbf{r}_{j,\beta}, h), \tag{18}$$

where the Kronecker delta is defined as

$$\delta_{\alpha,\beta} = \begin{cases} 1 & \alpha = \beta \\ 0 & \alpha \neq \beta \end{cases} \tag{19}$$

and α and β denote the state of a particle (in the sense of a color function) that can either belong to the fluid or solid region. Now, a proximity ratio can be defined as

$$\phi_i = \frac{n^s_i}{n_i}, \tag{20}$$

where n_i is the actual number density of a particle. For fluid and solid phases separated by a flat interface, this ratio is given by

$$\phi_i = \begin{cases} 0.5 & x_i = 0 \\ \in (0.5, 1) & 0 < x_i < h \\ 1 & x_i \geq h \end{cases}, \tag{21}$$

where x_i is the distance to the nominal surface, which is located at a distance equal to half of the interparticle spacing $\Delta x = (m/\rho)^{1/3}$ normal to the interface. To enforce a no-slip boundary condition, we return fluid particles along the normal to the fluid interface back into the flow domain once these particles penetrate the boundary, i.e., for $\phi_i < 0.5$. The surface normals are calculated using a color function:

$$c_i = \sum_{j=1}^{N} \frac{m_j}{\rho_j} \psi_j W(\mathbf{r}_{ij}, h), \tag{22}$$

where $\psi_j = 1$ for fluid particles and zero for solid particles, such that the surface normals can be obtained from the gradient

$$\hat{\mathbf{s}}_i = \nabla c_i \,. \tag{23}$$

Particles that penetrate the boundary are returned along the normal direction by a distance Δd proportional to the proximity ratio and have their velocity set to zero:

$$\Delta d = \beta \Delta x (1 - \frac{\phi_i}{0.5}), \tag{24}$$

where we have found $\beta = 1.0$ affords the best results for various values of surface tension and wall geometries. As noted in *Holmes et al.* [2011], the determination of the state number density via Eq. (18) may be subject to a slight error because of the kernel truncation

at the free surface. As such, higher values of β may be necessary to avoid penetration. The bounce-back condition is only activated when fluid particles initially come into contact with a solid boundary and fluid-solid interaction forces create a strong acceleration toward the solid wall. Generally, the forces created by the pressure gradient and repulsive part of the interaction in Eq. (11) are sufficient to keep particles from penetrating the wall boundaries. In addition, we extrapolate the smoothed fluid particle velocities to the adjacent boundary particles [*Adami et al.*, 2012]:

$$\mathbf{v}_i = -\frac{\sum_j \mathbf{v}_j W(\mathbf{r}_{ij}, h)}{\sum_j W(\mathbf{r}_{ij}, h)}, \tag{25}$$

such that in the absence of moving wall particles, the viscous interaction in Eq. (11) imposes a no-slip boundary condition. Solid walls consist of three layers of particles for W to satisfy the unity condition in Eq. (6) when fluid particles interact with the boundary particles.

2.2.8 Surface tension and contact angle

The force $\mathbf{F}^I_{ij}$ is constructed from two superposed cubic spline functions [*Kordilla et al.*, 2013] of the form

$$W(q,h) = \alpha_k \begin{cases} 1 - \frac{3}{2}(q)^2 + \frac{3}{4}(q)^3 & 0 \le q < 1 \\ \frac{1}{4}(2-q)^3 & 1 \le q < 2 \\ 0 & 2 \le q, \end{cases} \tag{26}$$

where $q = 2r/h$, such that

$$\mathbf{F}^I_{ij} = s\left[AW_1(r_{ij}, h_1) - BW_2(r_{ij}, h_2)\right]\hat{\mathbf{e}}_{ij}\,. \tag{27}$$

Here, $A = (h_1/h_2)^3 = 8$, $B = 1$, $h_1 = h$, $h_2/h_1 = 2$, and $\alpha_k = 1/\pi h^3$ to satisfy the unity condition. The force strength coefficient s is set to s_{ff} for interaction between two fluid particles and s_{sf} for interaction between fluid and solid particles. For the fluid to be wetting, s_{ff} should be smaller than s_{sf}. The surface tension can be calculated by employing the Young-Laplace law and the virial theorem to obtain the virial pressure [*Tartakovsky and Meakin*, 2005a; *Kordilla et al.*, 2013], and the contact angle can be measured from simulating a droplet on a flat solid surface. As recently demonstrated by *Tartakovsky and Panchenko* [2016], the surface tension and contact angle can also be analytically computed for any given shape of the interaction force. The presented formulation of SPH has several advantages for modeling free surface flows and contact angle dynamics: (1) it does not

require tracking the liquid-air and liquid-air-solid interfaces, and the interfaces "advance" with SPH particles; (2) the surface tension and contact angle are imposed via summation of $\mathbf{F}^I_{ij}$, i.e., there is no need to directly impose the Young-Laplace law, which requires estimation of normals and curvatures; (3) unlike multiphase models based on level Set, phase Field, and volume of fluid methods, SPH does not require explicit modeling of the air phase, which is not necessary when the air phase is continuous, resulting in a significant computational cost reduction; and (4) it accurately models both static and dynamic contact angles [*Kordilla et al.*, 2013; *Tartakovsky and Panchenko*, 2016] without defining empirical relationships between the contact angle and contact line velocity.

2.2.9 Time integration

Equation (11) is integrated using a modified Velocity Verlet time-stepping scheme [*Ganzenmüller et al.*, 2011]. Noting that

$$\frac{d\mathbf{r}_i}{dt} = \mathbf{v}_i \qquad \text{and} \qquad \mathbf{a}_i = \frac{\mathbf{f}_i}{m_i}, \tag{28}$$

where $\mathbf{a}_i$ is the acceleration. The time-stepping scheme is given as

$$\mathbf{v}_i(t + \tfrac{1}{2}\Delta t) = \mathbf{v}_i + \tfrac{1}{2}\mathbf{a}_i(t), \tag{29a}$$

$$\bar{\mathbf{v}}_i(t + \Delta t) = \mathbf{v}_i(t) + \Delta t \mathbf{a}_i, \tag{29b}$$

$$\mathbf{r}_i(t + \Delta t) = \mathbf{r}_i(t) + \Delta t \mathbf{v}_i(t + \tfrac{1}{2}\Delta t) \tag{29c}$$

$$\mathbf{v}_i(t + \Delta t) = \mathbf{v}_i(t + \tfrac{1}{2}\Delta t) + \frac{1}{2}\mathbf{a}_i(t + \Delta t)\,. \tag{29d}$$

After the calculation of new positions $\mathbf{r}_i(t + \Delta t)$, the extrapolated velocity $\bar{\mathbf{v}}_\mathbf{i}$ is used to compute the new particle acceleration $\mathbf{a}_i(t + \Delta t)$. Time step constraints are given by *Tartakovsky and Meakin* [2005a]:

$$\Delta t \leq 0.25h/3c \tag{30}$$

$$\Delta t \leq 0.25\min(h/3 \mid \mathbf{a}_i \mid)^{1/2} \tag{31}$$

$$\Delta t \leq \min(\rho_i h^2/9\mu_i), \tag{32}$$

where $\mid \mathbf{a}_i \mid$ is the magnitude of acceleration $\mathbf{a}_i$.

2.2.10 Model initialization

To initialize simulations, particles are placed on a grid with lattice size Δx. The kernel support is then computed as

$$h = N^{1/3}\Delta x\,, \tag{33}$$

and the particle mass is set to

$$m = \rho_0 h^3/N\,. \tag{34}$$

In this case, the number density, i.e., the amount of particles within a volume h^3, is defined as

$$n = \frac{N}{h^3}\,. \tag{35}$$

In our model, we set $N = 40$, which was shown to yield sufficient numerical accuracy for free surface flows, including the effect of pairwise interaction forces [*Tartakovsky and Meakin*, 2005a,b; *Kordilla et al.*, 2013]. It should be noted that some SPH parameters (s_{sf}, s_{ff}, c_0) are resolution dependent as the mass of a single particle scales with the particle spacing as $m = \rho_0\Delta x^3$ (in a three-dimensional system). However, the resulting fluids have bulk properties of water, independent of the chosen resolution.

3 Validation of the SPH code

To validate our code three experiments are carried out. First, we validate the code against an analytical solution for the droplet height. Then, we validate the code against experimental data for flow regime transitions, and, finally, we compare numerical and experimental data for the droplet dynamics at fracture intersections. Table 1 provides a list of the input parameters used for the simulations in this section and the following results section. The simulated fluid for all simulations is water at a temperature of 20 °C and surface tension $\sigma = 0.072\,\mathrm{kgs}^{-2}$. In all simulations, the viscosity is $\mu = 0.001\,\mathrm{kgm}^{-1}\mathrm{s}^{-1}$, and the solid reference density is $\rho_{s,0} = 1000.0\,\mathrm{kgm}^{-3}$.

3.1 Droplet height

The PF-SPH model with the bounce-back boundary condition has been validated under both dynamic and static conditions [*Kordilla et al.*, 2013; *Tartakovsky and Meakin*, 2005b; *Tartakovsky and Panchenko*, 2016]). Here, we present a numerical experiment to determine maximum droplet heights and compare it with an analytical solution to validate the PF-SPH model with the modified boundary condition. We model water at 20 °C at

Table 1. Parameters used in the simulations at each resolution. Additional constant parameters are introduced in the beginning of this section.

Δx (m)	$\rho_{f,0}$ ($\mathrm{kgm^{-3}}$)	s_{ff} ($\mathrm{kg\,m\,s^{-2}}$)	s_{sf} ($\mathrm{kg\,m\,s^{-2}}$)	c_0 ($\mathrm{m\,s^{-1}}$)
5.0×10^{-5}	950.0	2.0×10^{-7}	1.25×10^{-7}	18.0
1.0×10^{-4}	950.0	6.5×10^{-6}	2.0×10^{-6}	4.0
2.0×10^{-4}	930.0	1.3×10^{-5}	4.0×10^{-6}	2.5
3.0×10^{-4}	930.0	2.0×10^{-5}	6.0×10^{-6}	2.0
4.0×10^{-4}	930.0	2.5×10^{-5}	7.0×10^{-6}	1.75
5.0×10^{-4}	930.0	3.0×10^{-5}	8.0×10^{-6}	1.5

three different resolutions $\Delta x = 1.0 \times 10^{-4}$ m, $\Delta x = 2.0 \times 10^{-4}$ m, and $\Delta x = 5.0 \times 10^{-4}$ m. Table. 1 features the corresponding paramters for all cases. In all simulations, the fluid viscosity is set to $\mu = 0.001\,\mathrm{kgm^{-1}s^{-1}}$, and the surface tension is $\sigma = 0.072\,\mathrm{kgs^{-2}}$.

Sessile droplets assume a spherical cap shape when their radius r is small compared to the capillary length

$$\lambda_c = \sqrt{\frac{\sigma}{\rho g}}, \tag{36}$$

i.e., $r \ll \lambda_c$, whereas larger droplets tend to be flattened by gravitational effects that limit the maximum height h_{max}. The maximum height can be approximated by [*de Gennes*, 1985]:

$$h_{max} = 2\lambda_c sin\left(\frac{\theta_0}{2}\right), \tag{37}$$

where θ_0 is the static contact angle between the fluid and solid surface. Figure 3 (left) shows the maximum droplet height obtained for three different resolutions of our SPH model versus the droplet width. At both coarser resolutions, we obtain a good convergence to the theoretical solution. For the lower limit, when the droplet width approaches the capillary length of water, a constant height-to-width ratio can be recovered in accordance with spherical cap theory [*Harris and Stocker*, 1999] (Fig. 3, right).

3.2 Flow regime transitions

To validate the SPH model for a complex flow setting, we conduct a series of laboratory experiments to determine prevailing flow modes for various flow rates ranging from

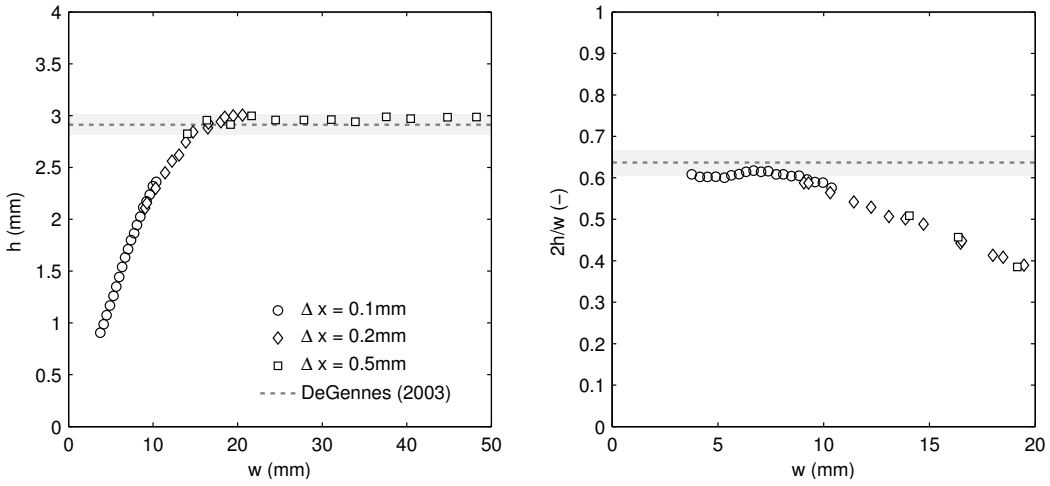

419 **Figure 3.** Droplet heights h for three resolutions and several droplet radii in terms of their width w (left).
420 Droplets with a radius much larger than the capillary length are flattened by the effect of gravity and establish
421 a maximum height, i.e., form fluid puddles. For smaller droplet sizes, approaching the capillary length of wa-
422 ter, a constant ratio of width to droplet height can be recovered in agreement with spherical cap theory (right).
423 Shaded areas represent the standard deviation assuming an error of ±2.5° for the contact angle measurement.

433 1.5–4.5 mL min^{-1} at different resolutions on a smooth vertical surface. For the given fluid-
434 solid combination, the whole spectrum of flow modes (droplets, mixed droplets/rivulet,
435 rivulets) can be observed (Figure 4). Due to environmental "noise," such as slight im-
436 purities on the PMMA surfaces and/or tiny air pressure or flow rate variations [*Dragila*
437 *and Weisbrod*, 2004; *Wood and Huang*, 2015], it is nearly impossible to establish a per-
438 fect droplet regime, i.e., a stream of individual droplets moving at the exact same velocity
439 down the surface. Such interferences commonly induce mixed flow regimes, e.g., merging
440 droplets that temporarily form partial rivulets or larger droplets traveling at high velocities
441 and emitting smaller droplets.

442 While the transition to full rivulet flow can be easily determined (a continuous stream
443 is established), the intermediate regimes are rather difficult to compare quantitatively un-
444 der such conditions. The final transition from droplet flow mode to constant rivulet flow
445 mode is found to be at about 3.15 mL min^{-1} (±0.25 mL min^{-1}) for the laboratory experi-
446 ments and at 3.0 mL min^{-1} for the SPH simulations. Six different resolutions (Δx = 50,
447 100, 200, 300, 400 and 500 µm) with parameters given in Table 1 are tested, and conver-
448 gence is approximately found at a resolution of Δx = 100 µm. For lower resolutions, the

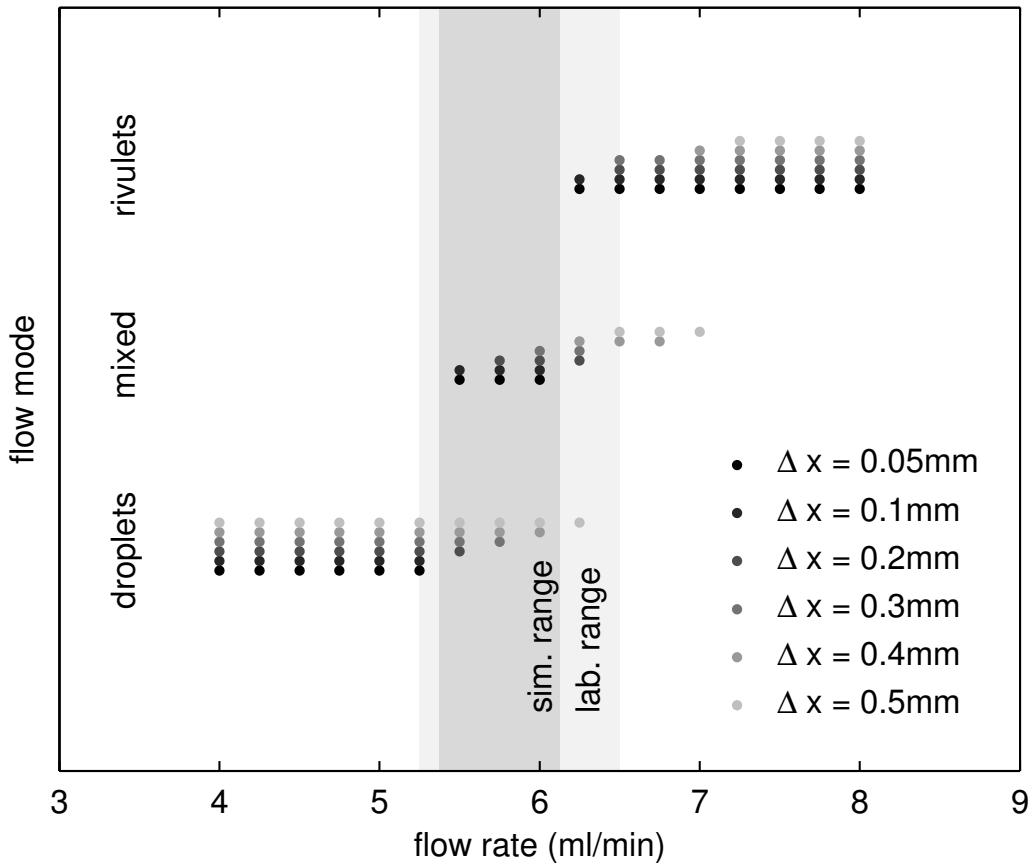

Figure 4. Convergence study for prevailing flow modes for various SPH resolutions (one simulation per data point). Gray zones indicate the range of the mixed flow regime for simulations and laboratory experiments.

transition to rivulet flow occurs at slightly higher flow rates. Depending on the resolution, the thickness of the rivulets in terms of particle numbers ranges from 51 at the highest resolution to about 6 particles at the lowest resolution.

Figure 5 shows a qualitative comparison of our SPH model for three different flow rates. All three cases (droplet mode, droplet-rivulet transition, and rivulet mode) are correctly reproduced by the model.

Flow regime transitions between the droplet and rivulet regime are reasonably well reproduced by the SPH model at a minimum resolution of $\Delta x = 1.0 \times 10^{-4}$. Furthermore, the model can reproduce the transitional regime, which requires resolving the singularity at droplet tails and/or merging interfaces. This process arises naturally in our SPH formulation and is required to fully understand the dependence of partitioning dynamics on

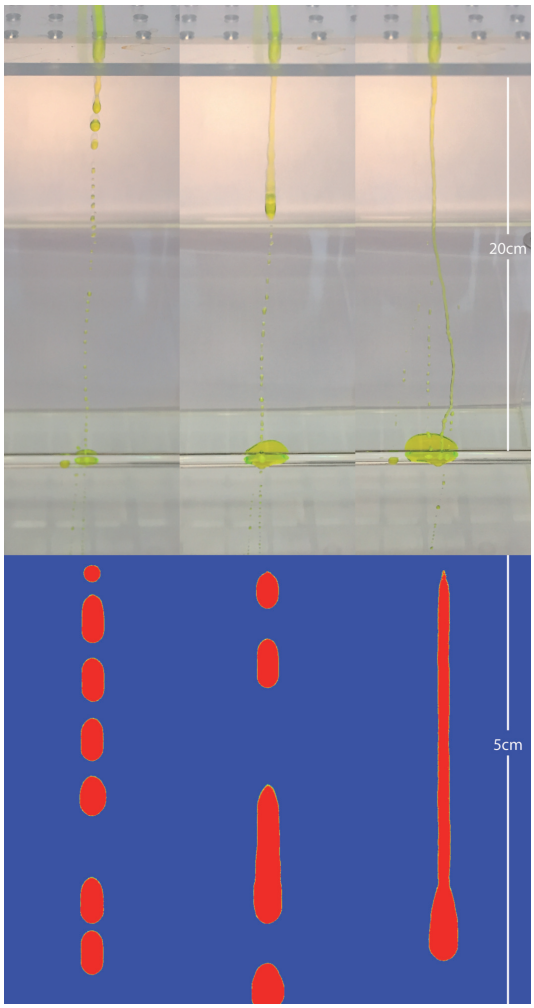

455 **Figure 5.** Flow mode transitions observed in the laboratory and corresponding SPH simulations.
456 (Left) Droplet mode at 1.5 mL min^{-1}, (middle) transition zone from droplet to full rivulet flow mode at
457 2.5 mL min^{-1}, and (right) constant rivulet mode at 4.5 mL min^{-1}. Note the difference in scale between sim-
458 ulations and experiments. Rivulets and droplets have an average thickness of 16 particles and 24 particles,
459 respectively.

flow modes at fracture intersections. Theoretically, a sharp transition between droplet and rivulet flow modes should occur [*Hasseine et al.*, 2011]. In both the laboratory experiments and SPH simulations, a transition range of mixed flow modes can be detected. This transition range is slightly smaller in the numerical experiments, as there is no influence of the environmental noise present in the lab experiments. However, it should be noted that even SPH simulations suffer from a certain noise component. Particles are injected randomly within a small injection region. Given a constant random seed for the random number generator, they are reproducible. However, they are not perfectly symmetric. This may prevent the formation of perfect, equally-sized droplet trains.

3.3 Droplet dynamics at a horizontal fracture intersection

To validate the model under dynamic conditions, we investigate the behavior of individual sliding droplets across a fracture intersection. Droplets are expected to exhibit a fractionation or partitioning behavior at the intersection. They may not wholly or partially (i.e., leave behind some fluid mass in the horizontal fracture) bypass the fracture. The experimental setup for this validation study is similar to the one depicted in Figure 2, except for the inlet, which is now placed at a distance of 5 cm above the horizontal fracture. This distance is sufficient for droplets to reach constant velocity before encountering the fracture. Droplets are manually placed on the vertical surface with an Eppendorf pipette.

The droplet volume V_d and fracture aperture are varied during the experiment, where V_d = 25, 30, 35, 40, 45 and 50 µl and d_f = 0.35, 0.7, 1.0, 1.4, 2.0 and 2.5 mm. For each combination, we conduct 10 experiments to account for environmental noise, slight changes during the injection process, and potential impurities on the surfaces. To quantify the fractionation behavior at the fracture intersection, we distinguish between two cases: (1) droplets bypass the intersection and exhibit ongoing movement, where some fluid mass may get trapped within the fracture, or (2) droplets are stuck at or within the fracture intersection. In certain cases, fluid may slightly bypass the fracture but not show any ongoing movement on the lower vertical surface. Such cases are counted as "stuck." Figure 6 illustrates the described cases as simulated by our code, where only case (a) is counted as a bypass. For each parameter combination, we run one simulation at a resolution of $\Delta x = 1.0 \times 10^{-4}$ m and parameters given in Table 1. Droplets consist of 27.000 to 54.872 particles with an average thickness of 22 to 29 particles.

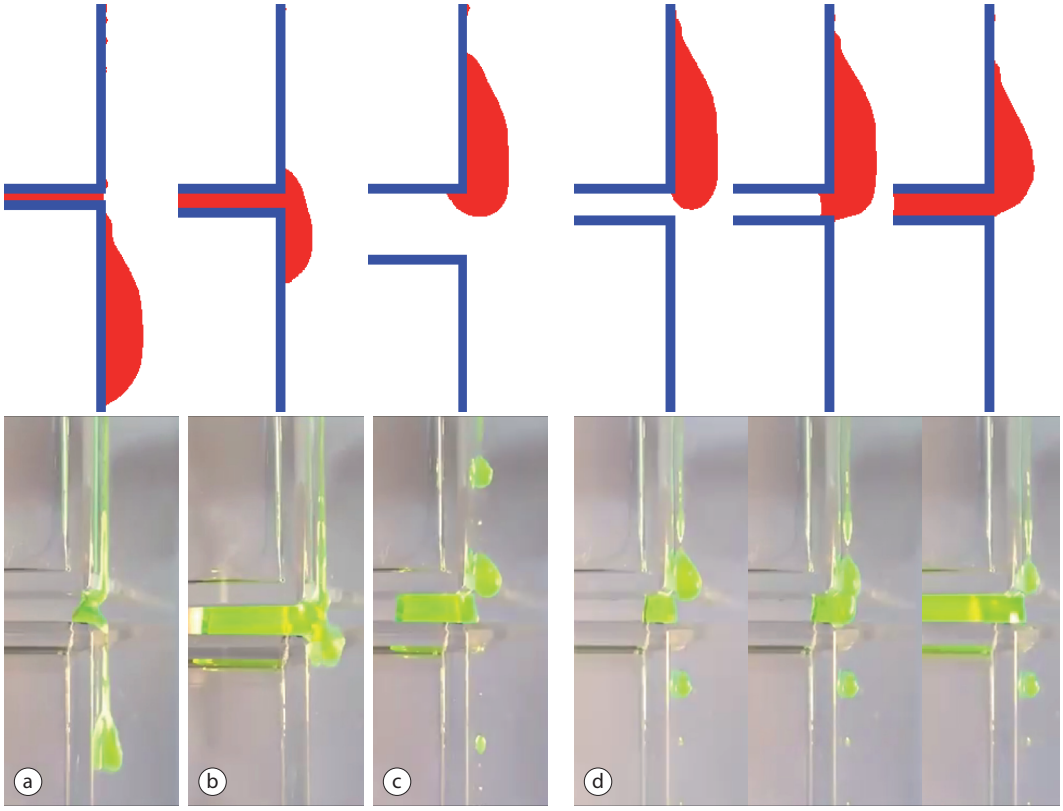

Figure 6. General cases of the fractionation process: (a) Full bypass of a droplet and ongoing movement. (b) Bypass with or without snapping of the droplet but no ongoing movement. (c) Droplets are stuck and may partially move into the fracture along the upper fracture wall. (d) Sequence of three frames. No bypass occurs. Droplets establish a connection to both fracture walls and are fully trapped within the fracture by capillary forces.

Figure 7 shows the results of the laboratory experiments and SPH simulations. Generally, good agreement is observed. The laboratory experiments exhibit a transition region where only some droplets bypass the fracture. We conduct only one simulation for each case, and our numerical results cannot exactly describe the transition zone. However, in the simulations, we distinguish a third case (see Fig. 6b), where a droplet partially bypasses the fracture but does not show any ongoing movement. This case occurs only within the transition region, where such behavior is to be expected. Droplet heights (normal to the vertical surface) have been measured experimentally and yielded a maximum of around 2.47 mm, which is close to the aperture of the horizontal fracture.

We find a good agreement between SPH simulations and laboratory experiments. The setup allows a well-controlled droplet size in contrast to the highly dynamic single-

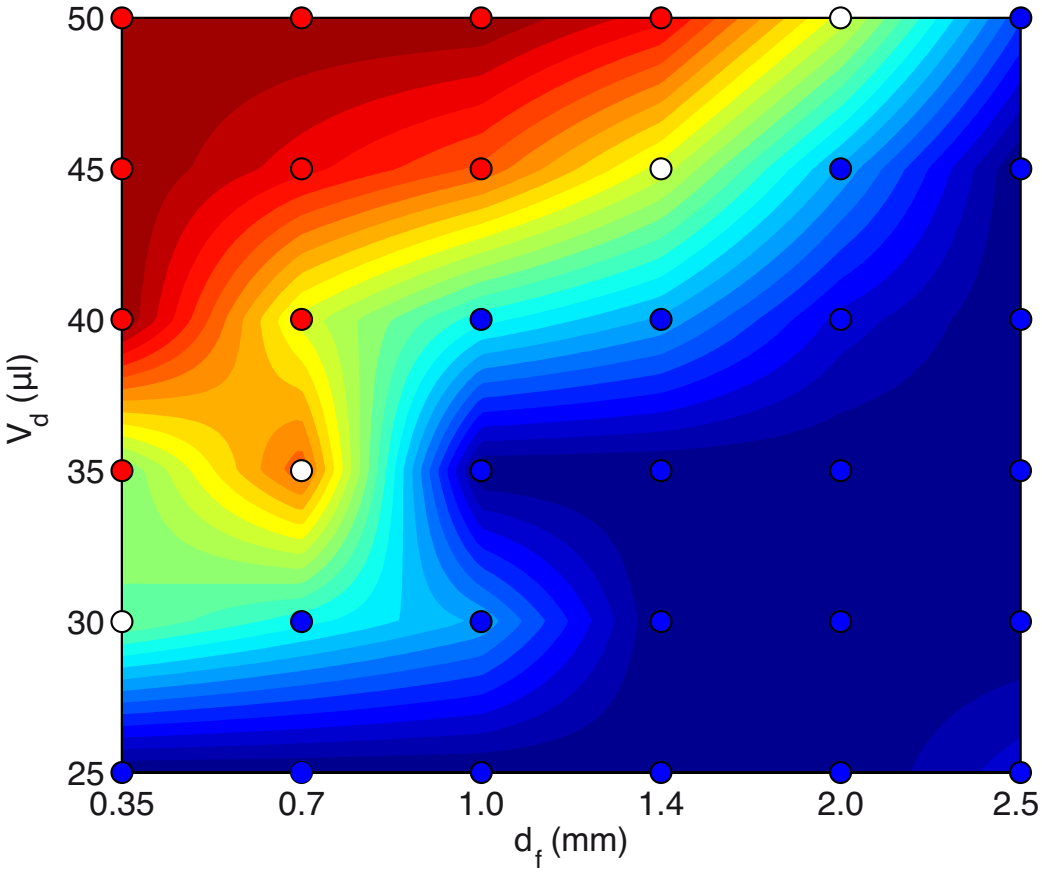

Figure 7. Experimental results are shown as contours. For each combination of fracture aperture d_f and droplet volume V_d, 10 experiments are carried out. Colors are mapped to the ratio of bypassing and total droplets, where red = 1 and blue = 0. For each combination, one simulation is run, where red markers indicate bypass, blue markers trapped droplets, and white markers a case of partial bypass (but no further movement; see also Figure 6b).

and multi-inlet experiments, where a complex and erratic combination of droplet sizes and shapes (mixed droplet-rivulet shapes, e.g., elongated droplets) characterizes the transient flow field. The experiment demonstrate that single droplets, independent of the investigated size, are unlikely to bypass the fracture for fracture apertures above ~2.0 mm. This result is somewhat surprising as transient flow experiments in Section 4.2 (horizontal fracture aperture of 2.5 mm) reveal that droplet-regime-dominated flows possess a strong bypass capacity, specifically during the early stages of the experiment, when the horizontal fracture is still dry. This indicates that the effects of dynamic droplet merging and consequently the intermediate formation of larger droplets (also referred to as "snapping rivulets," e.g., *Dragila and Weisbrod* [2003]) are an important aspect of the partitioning dynamics, which are not reflected in this experiment.

4 Results

In this section, we present the numerical and experimental results of droplet and rivulet flow partitioning in a single fracture. As described in Sec. 2.1 we first investigate the partitioning dynamics for a single inlet to elucidate the relation between flow regime and flow partitioning. Then, we study a multi-inlet system to obtain an integrated view of the flow partitioning, which can be compared to analytical and numerical estimates. These results are discussed in the following section.

4.1 Single-inlet partitioning dynamics

Figure 8 shows the ratio of bypassing fluid mass M_b versus total injected mass M after 90 s. It is apparent that at flow rates of 3.0 mL min^{-1} or higher, nearly no fluid bypasses the horizontal fracture (until it is fully wetted). At lower flow rates, the likelihood of bypass increases. On the other hand, in the transition zone between full droplet and rivulet mode, the experiments exhibit a rather high variance with an increasing average value for decreasing flow rates. Considering the complex pattern of droplet splitting, coalescence, and temporary rivulet formation, this is to be expected.

While these results already highlight the importance of flow modes for percolation dynamics through fracture networks, the high variance of the results, especially for lower flow rates in the droplet flow regime (see *Wood and Huang* [2015]), makes it difficult to compare results to simulation data and obtain an analytical solution. Therefore, in the fol-

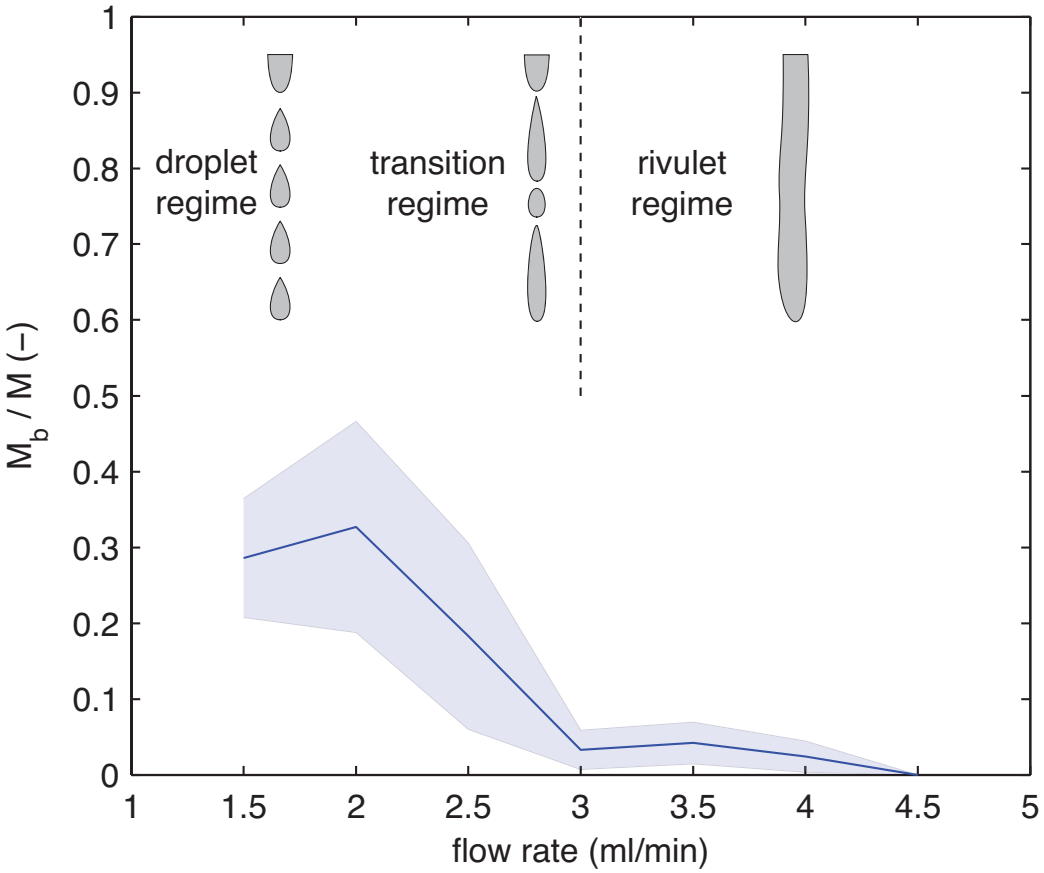

Figure 8. Ratio of bypass mass versus total fluid mass after 90 s for a single-inlet experiment. Blue line = mean of 10 experiments at each flow rate. Shaded area = standard deviation. The partitioning behavior at the fracture intersection can be clearly linked to the occurrence of flow modes on the vertical surfaces. For rivulet flows, nearly all injected water is stored in the horizontal fracture. In the droplet flow regime, water predominantly bypasses the fracture. While in the droplet-rivulet transition zone an increase of bypass efficiency with increasing droplet count (or decreasing rivulet amount) is observed.

lowing section, we extend our laboratory experiments and SPH simulations to include a larger number of inlets.

4.2 Multi-inlet partitioning dynamics

Figures 10 and 11 show the qualitative results of the laboratory experiments and the corresponding SPH simulations. The numerical simulations are setup with an interparticle spacing of $\Delta x = 500\,\mu\text{m}$ (parameters given in Tab. 1) and consist of approximately three

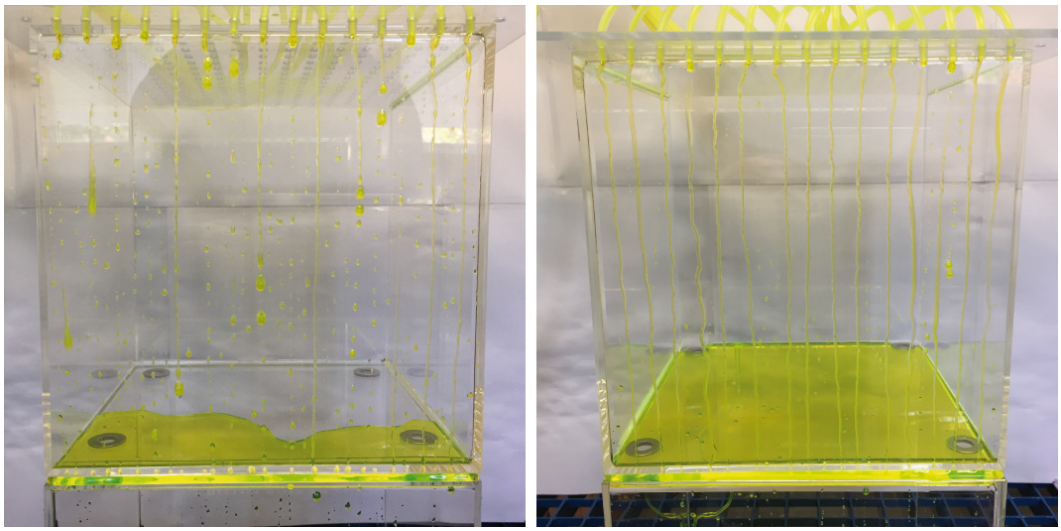

Figure 9. Droplet mode (left) and rivulet regime (right) for different total flow rates. To keep the same total flow rate in both experiments and establish stable rivulets, the number of inlets is reduced in the final experiments (i.e., the flow rate per inlet is increased). Dye was added for better visibility.

million particles. Individual flowing droplets consist of about 200 to 750 particles with a thickness between 4 to 8 particles.

Figure 12 shows the fluid mass accumulation over time for the laboratory experiments and SPH simulations. For each injection scenario (droplet versus rivulet), we carry out 20 experiments and take the ensemble average. The SPH simulations are in good agreement with the averaged experimental results — except for a transition period of about 50 s, where simulated mass accumulation is within one standard deviation from the averaged mass accumulation observed in the experiments and always within the maximum and minimum of experimentally observed values.

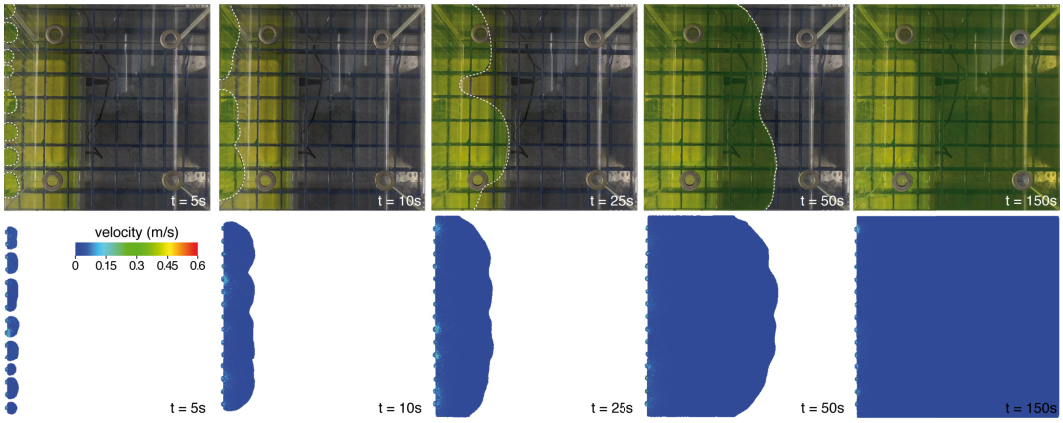

574 **Figure 10.** Top view of the laboratory experiment with droplet flow (top) and the SPH simulations (bot-
575 tom).

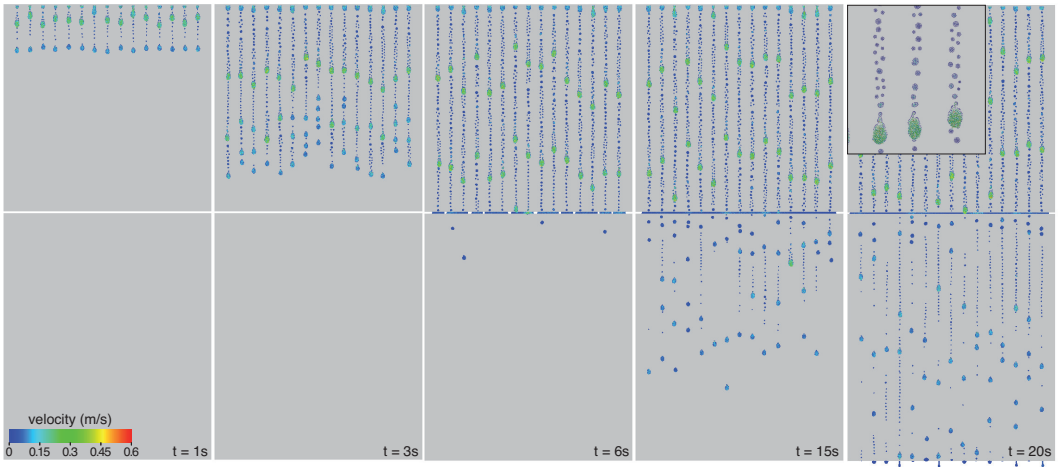

576 **Figure 11.** Frontal view of a point-wise injection simulation at a resolution of $\Delta x = 5.0 \times 10^{-4}$ m and about
577 three million particles. The inset shows a detailed view of droplet trails. At the chosen resolution, flowing
578 droplets are resolved by an average of 200 to 750 particles and have a thickness of 4 to 8 particles.

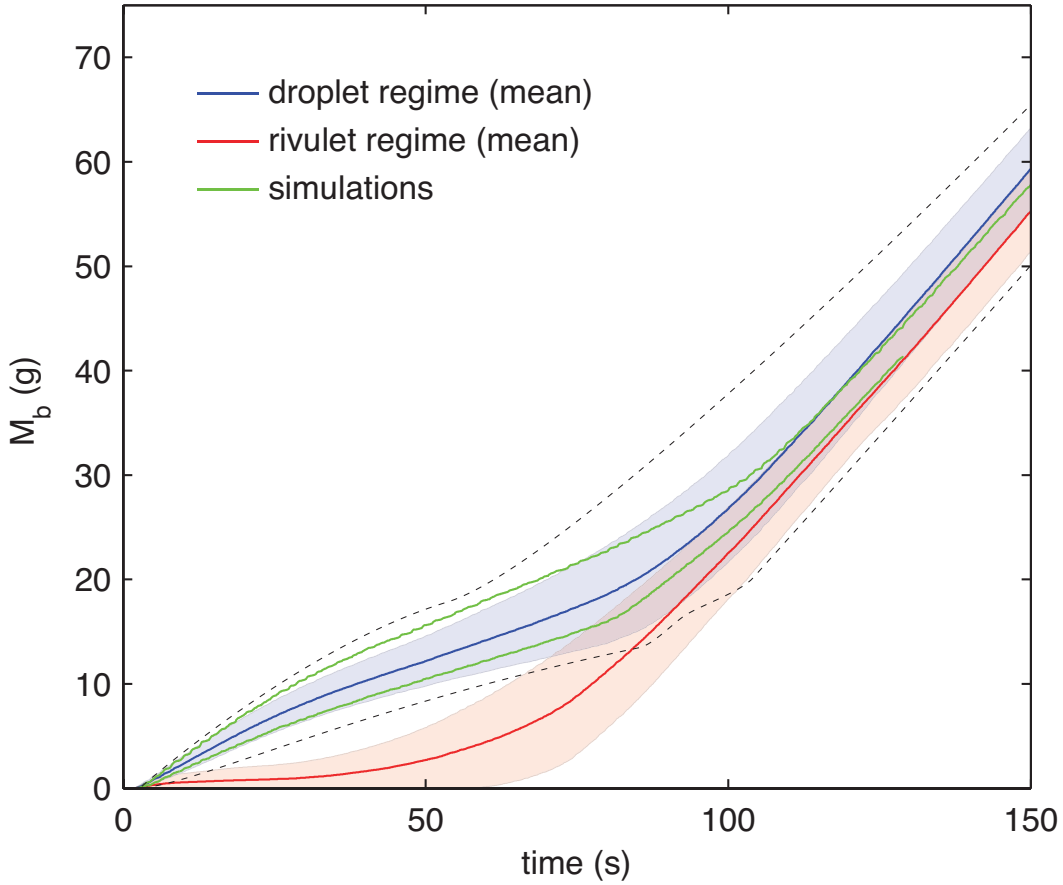

Figure 12. Comparison of mass accumulation (bypassed fluid mass M_b) at the system outlet for two injection schemes and SPH simulations. Shaded areas represent the standard deviation and dashed lines the maximum and minimum hull for the droplet regime experiments. Droplet regime experiments exhibit an earlier first arrival, while the rivulet regime experiments display a stronger flow into the horizontal fracture and consequently a delayed first arrival.

5 Discussion

In the following, we discuss the experimental outcomes reported in the previous section. Special attention is paid to understanding of global or bulk dynamics in the context of multi-inlet dynamics, and an analytical solution based on the Washburn equation is presented to cast results into a physical framework. Finally, we discuss possible deviations from natural systems due to the simplified conceptual model.

5.1 Single-inlet partitioning dynamics

While the previously discussed experiments mainly serve as a validation base for our code, the complex transient laboratory experiments (Section 4) provide a basis for better understanding of bulk behavior. The single-inlet experiments indicate a clear dependence of the partitioning dynamics at fracture intersections on the flow mode after a duration of 90 s. At high flow rates, well within the rivulet dominated regime, bypass rates reach a minimum (accompanied by very low variance in experimental outcomes). This can be explained by the lower height of rivulets (normal to the vertical surface) compared to droplets, which prevents gravitational movement across the fracture aperture. Instead, rivulets that arrive at the fracture intersection directly move horizontally into the fracture, where the initial contact is established along the upper horizontal fracture wall, and in most cases, immediately followed by contact with the lower horizontal wall. Slight overshoots can be observed for rivulets as well (Fig. 6b). However, because of capillary drag on the (infinite) rivulet tail by the fracture, these are nearly always pulled back into the fracture. For decreasing flow rates, i.e., within the transition range between droplet and rivulets, we observe a constant increase in bypass rates, owing to the increased number of individual droplets that are emitted either directly at the injection inlet or at the tail of larger droplets (slugs) and are able to bypass the fracture. For the given setup, the maximum bypass rate is established when the flow mode switches to pure droplets. Here, the stream consists entirely of droplets, which may temporarily merge with low Bond number droplets stuck on the surface and thus exceed the critical volumes required to bypass the fracture. The single-inlet experiments mainly provide qualitative insight into the partitioning behavior. However, because of the long timescales required to reach equilibrium conditions and the rather high variance, they are not suitable to investigate the bulk system response.

5.2 Multi-inlet partitioning dynamics

The multi-inlet experiments provide a much better view of the global bulk dynamics. While we employ both injection schemes in the laboratory, SPH simulations are only carried out for the case of a droplet flow regime. As demonstrated in Section 3.2, a resolution of $\Delta x = 100\,\mu\text{m}$ is required to sustain stable rivulets. At this resolution, simulations of flow with multiple injection points will consist of ~0.5 billion particles. While our computational resources are sufficient to run the code on several thousand cores, for such high resolutions, the increasing constraints on the time step caused by the compressibility criteria and the choice of speed of sound (see Eq. 30) would aggravate or render absolute simulation times $t > 100\,\text{s}$ impossible. Therefore, multi-inlet SPH simulations are conducted only for the case of point injections, where flow is dominated by individual droplets.

As demonstrated in Section 4.1 and discussed before, the main difference between both flow regimes (rivulet and droplet) in terms of partitioning behavior, can be attributed to the bypass efficiency of the prevailing flow mode. For rivulet regime experiments and simulations, the initial fluid mass is almost entirely stored within the horizontal fracture until a critical threshold is reached at about 30 s (see Fig. 12). Then, fluid reaches the system outlet at an increasing rate until an equilibrium is reached, i.e., the horizontal fracture is completely filled. Droplet flows have an earlier arrival time because, initially, the horizontal fracture is easily bypassed, which is consistent with the single-inlet experiments. At about 15 s, the efficiency temporarily drops until at about 90 s when a transition to equilibrium state is initiated.

To quantitatively analyze the flow partitioning and flow dynamics, we consider the mass flux into the horizontal fracture. Thus, we recall that the total injected fluid mass is

$$M(t) = Q_0 t, \tag{38}$$

where Q_0 ($\text{L}^3\,\text{T}^{-1}$) is the volumetric flow rate and t is the time. From the previous experiments, it is apparent that the horizontal fracture acts as a buffer, i.e., the fluid mass is partitioned between two components

$$M(t) = M_f(t) + M_b(t), \tag{39}$$

where M_f is the fluid mass within the horizontal fracture and M_b refers to the fluid mass that bypasses the fracture. The total volumetric flow rate then becomes

$$\frac{dM(t)}{dt} = Q_0 = \frac{dM_f(t)}{dt} + \frac{dM_b(t)}{dt}. \tag{40}$$

Thus, the volumetric flow rate into the fracture is

$$Q_f(t) \equiv \frac{dM_f(t)}{dt} = Q_0 - \frac{dM_b(t)}{dt}. \tag{41}$$

Figure 13 illustrates the normalized flow rate Q_f/Q_0 in the fracture for the rivulet- and droplet-dominated flow conditions. The experimental data for the rivulet flow indicate that in the early penetration phase, water creeps along the horizontal fracture walls, reflected by the increase in the flux into the fracture. At around 10 s, the flux becomes constant and is essentially equal to the applied water flux. Then, at around 20 s, the flux decreases slowly until $t \approx 60$ s, after which it decreases exponentially fast. The slow decrease in the time window between $t = 20$ s and 60 s can be understood as a Washburn flow regime [*Washburn*, 1921] that starts once a coherent water front has been established.

We observe similar behavior for the droplet-dominated experiments, where the initial filling of the fracture cannot be simply approximated by plug flow. Initially, the front emerges as isolated "puddles" (see Fig. 10 , $t = 5$ s), and the initial filling rate depends on the merging rate of these puddles. As in the rivulet flow regime, once a continuous fluid front is established, the force balance at the fracture intersection is influenced by the strong capillary drag of the fluid into the horizontal fracture, and the gravity-driven bypass of droplets is impeded. Similar to the rivulet-dominated flow experiments, we observe a Washburn-type flow regime, which is characterized by a $\sqrt{t}$ advance of the fluid front.

When a continuous fluid front is established in the fracture, flow is dominated by capillary forces. Following *Washburn* [1921], a Poiseuille flow develops between the fracture planes that is driven by the capillary pressure drop over the penetration length $l(t)$. The pressure gradient decreases as the front moves into the fracture [*Washburn*, 1921; *Alava et al.*, 2004]. Thus, combining Poiseuille's law for a planar fracture with the expression for the differential fluid volume in the element of length $dl(t)$ gives the length $l(t)$ of the invading water front

$$\frac{dl(t)}{dt} = \frac{c_f}{l(t)}. \tag{42}$$

The constant c_f can be defined by

$$c_f = \frac{\Delta P_c}{\mu}\frac{d_f^2}{4}, \tag{43}$$

where d_f is the fracture aperture and the capillary pressure ΔP_c is given by

$$\Delta P = \frac{2\sigma cos(\theta)}{d_f}\,. \tag{44}$$

The solution of Eq. (42) for the initial length $l(t = t_0) = l_0$ gives

$$l(t) = \sqrt{l_0^2 + 2c_f(t - t_0)}. \tag{45}$$

For a uniformly advancing front, the fluid mass within the fracture is $M_f(t) = A_f l(t)$, where A_f is the cross-sectional area of the fracture. Thus, the flow rate into the fracture can be obtained according to Eq. (41)

$$Q_f(t) = A_f \frac{dl(t)}{dt} = \frac{Q_0}{\sqrt{1 + 2k_f(t - t_0)}}, \tag{46}$$

where we set $A_f c_f / l_0 = Q_0$ and $k_f = c_f / l_0^2$. This expression gives the characteristic $t^{-1/2}$ behavior indicated by the solid black line in Figure 13.

5.3 Experimental and conceptual limitations

To isolate the fundamental processes and decrease the variance of experimental outcomes, it is often necessary to design simplified models of natural systems. Our experimental setup deviates from true geological systems in several aspects, such as it uses flat surfaces. Natural fractures have a roughness that develops over several length scales [*Bouchaud*, 1997; *Ponson et al.*, 2006], ranging from macro-roughness (in a sense of a tortuosity) to micro-roughness, which may even invalidate using macroscopically defined contact angle models or classical no-slip boundary conditions (e.g., in the case of a Lotus-effect-like roughness). While the chosen contact angle of about 65° is within the range of (a limited selection) of literature values between 23° and 70° *Su et al.* [1999]; *Sobolev et al.* [2000]; *Tokunaga and Wan* [2001]; *Su et al.* [2001], it is most likely at the upper range of contact angles.

The setup geometry obviously favors the conceptual idea of wide vertical apertures intersected by sub-vertical fractures. While we have not investigated the effect of changing fracture topology and/or fracture aperture, these are likely to affect results. In the following, we discuss possible effects of: (1) different apertures, (2) different angles, and (3) fracture roughness. As demonstrated in Section 3.3, the horizontal fracture aperture prevents bypass of single droplets nearly entirely for apertures above 2.0 mm. In contrast, for the transient single- and multi-inlet dynamics, a stronger bypass of droplets is observed due to dynamic emittance, the merging and consequently temporary formation of

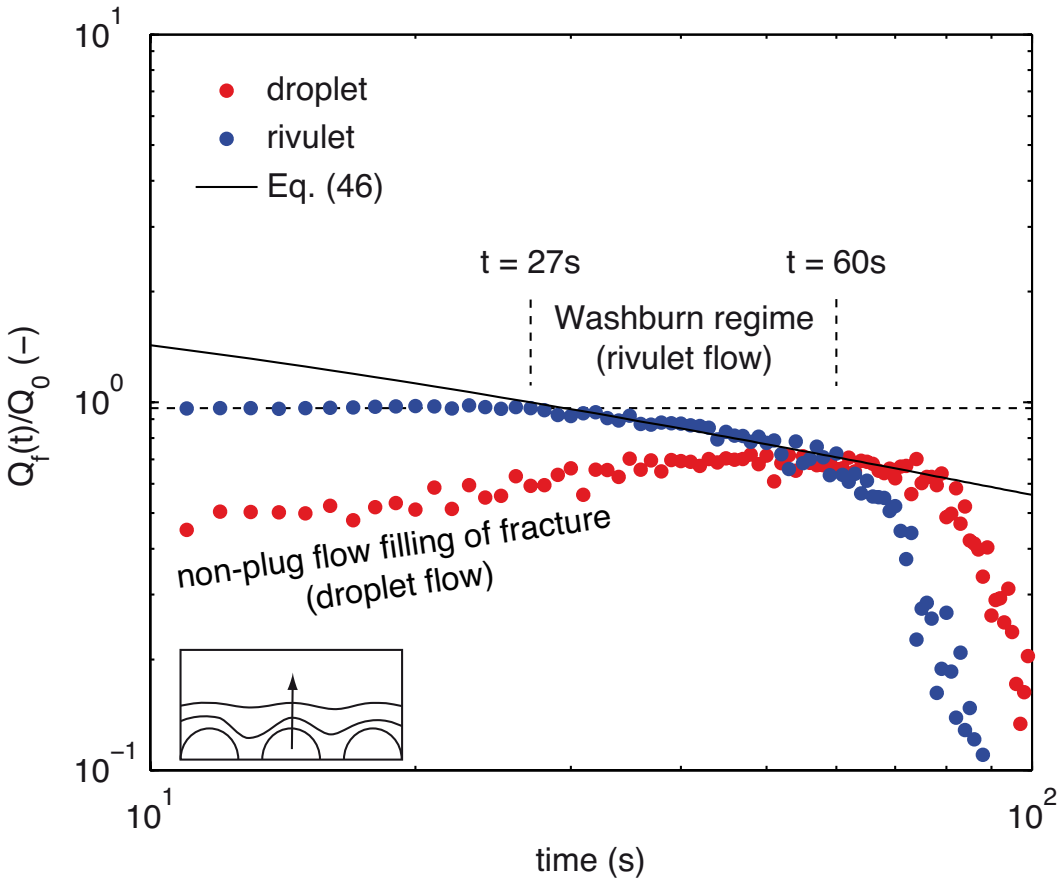

672 **Figure 13.** Normalized flow $Q_f(t)/Q_0$ in the fracture. The dashed line denotes the plug flow regime, and
673 the solid line denotes expression Eq. (46) for $t_0 = 27$ and $k_f = 0.015\,\mathrm{m^2 s^{-1}}$. The inset shows the effect of
674 progressing fluid front closure, which explains the increased filling of the horizontal fracture for droplet flows
675 until the Washburn regime is reached at around $t = 65$ s.

large elongated droplets, even for an aperture of 2.5 mm. For smaller horizontal fracture apertures, the bypass efficiency will increase. At the same time, the fracture volume and capillary drag increases, so the effect on the onset of the Washburn regime (at time t_0) is ambiguous. Further experiments would be required to clarify this behavior. The (infinite) aperture of the vertical fracture in our setup allows the formation of gravity-driven free surface flows (droplets, rivulets, wavy films). A lower aperture limit, at which a capillary bridge to an opposing fracture wall can be established, depends on various parameters, such as (dynamic) contact angles, Capillary-Bond number scaling relationships [*Podgorski et al.*, 2001], and fluid properties as these control the thickness of prevailing flow modes. Given a capillary connectivity to a second fracture wall, the impact of gravitational forces will obviously decrease and the force balance will switch to a capillary-dominated regime for fracture apertures below about 0.7 mm [*Wood et al.*, 2005]. In this case, the efficiency of the horizontal fracture to store water will increase because of the decrease in vertical flow velocities.

The orientation of the fractures (both horizontal and vertical) influences the partitioning dynamics but should also be discussed in terms of bulk behavior, for example, in the context of fracture network connectivity and percolation. The orientation of the vertical fracture surface affects the bypass dynamics, mainly because of the change in flow velocities. In terms of dimensionless characterization, it is often assumed that scaling relationships in the form of

$$Ca \sim Bo \cdot sin(\alpha_s) - \Delta_\theta \tag{47}$$

hold for the simple case of droplet dynamics [*Podgorski et al.*, 2001; *Ghezzehei*, 2004; *Or*, 2008; *Kordilla et al.*, 2013], where the capillary number Ca is defined as

$$Ca = \frac{\mu v}{\sigma} \tag{48}$$

and the Bond number Bo as

$$Bo = \frac{V^{2/3}\rho g}{\sigma}\,. \tag{49}$$

Here, α_s is the inclination angle from the horizontal plane, Δ_θ controls the lower limit of $Bo \cdot sin(\alpha_s)$ under which droplets remain sessile, and V is the droplet volume. It is inferred that droplets assume a spherical cap shape, such that a change in surface orientation is equivalent to a change in Bond number, i.e., droplet size. While we have not provided a dimensionless analysis of the single droplet dynamics at a fracture intersection, the pre-

ceding relationships may provide a solid base to relate bypass dynamics to the geometrical properties of the fracture and wetting properties of the fluid-solid system.

The orientation of the horizontal fracture can be discussed in a similar fashion as for the previous case. A rotation toward the vertical fracture will induce additional gravitational drag on fluid entering the horizontal fracture, i.e., the capacity to store and release fluid will be limited and the Washburn regime may not even be established. However, a counterclockwise rotation will not only increase the imbibition efficiency but may also introduce an outlet condition, such that water may leave the horizontal fracture into a different vertical fracture. This second case introduces a completely different conceptual base, in a sense that the horizontal fracture will not act as limited storage, which ultimately always returns flow into the injection fracture.

Despite careful preparation of the laboratory equipment, the experiments may be affected by impurities and environmental noise. We cannot rule out that the synthetic surfaces have microscopic impurities, which may cause tiny fluctuations in the flow field and consequently erratic flow dynamics, specifically in the case of droplet flows. While *Dragila and Weisbrod* [2003] noticed that air pressure fluctuations have influenced the formation of droplet and rivulet modes, we have found no clear dependence on the air pressure in our experiments over the course of one month and a pressure range of 1000 to 1035 mbars. Our laboratory setup consists of very small 1-mm diameter injection tubes. We initially conducted experiments with slightly thicker injection inlets, which promote stronger formation of capillary droplets around the injection tube. This behavior relates to the work of *Or and Ghezzehei* [2000] who investigated dripping dynamics in cavities and found that the variations in experiments stem from the varied sizes of the injected droplets.

6 Summary and conclusions

Flow through unsaturated fractured systems strongly deviates from capillary-driven flow dynamics and is dominated by gravitational forces for high aperture fractures. Within the context of preferential flow dynamics, sub-horizontal wide aperture fractures form highly effective pathways intersected by horizontal fractures, which act as integrators with respect to the uptake and release of water [*Wood et al.*, 2002] and often create a (temporary) capillary barrier [*Ji et al.*, 2006; *Wood et al.*, 2005]. The partitioning dynamics at

these intersections is still poorly understood and influenced by a diverse range of boundary conditions.

In this work, we study unsaturated flow dynamics in a wide aperture system, composed of vertical open surface intersected by a wide aperture (2.5 mm) horizontal fracture, using a combination of numerical simulations, laboratory experiments, and an analytical approach.

We demonstrate that our three-dimensional SPH code is capable of simulating the challenging free surface flow dynamics, including effects of surface tension, on several hundreds of processors. The code is validated by comparison with analytical solutions and laboratory experiments, which cover a variety of flow modes that may occur in unsaturated fractures.

In accordance with previous studies, the horizontal fracture may act as a capillary barrier of varying efficiency, which stores and releases water. Our experiments highlight the flow-mode-dependent (droplet, rivulet, mixed-mode) behavior of the non-equilibrium partitioning dynamics at the fracture intersection until steady-state flow is established.

Droplet-dominated flows enhance the bypass efficiency at the fracture intersection, while rivulet flows produce a stronger buffering (uptake) of fluid within the horizontal fracture. For both cases, a temporary existence of a Washburn-type regime within the horizontal fracture is observed in the laboratory and numerical experiments and is described by an analytical solution. In the case of rivulet flow, the onset of this regime is preceded by a period of plug flow into the fracture with nearly no bypass occurring. For droplet flows, the initial filling slowly increases until a closed fluid front at the horizontal fracture inlet is established from individual, radially evolving imbibition spots, which then penetrate the fracture as a quasi-straight front.

In both cases, departure from the Washburn-type regime is observed when the negative fluid pressure, forcing fluid into the horizontal fracture, declines, and the fracture finally is fully saturated. While the existence of the Washburn regime is obvious, the times of onset and departure can be clearly linked to the specific flow mode and may be useful to obtain global system dynamics, which incorporates classical flow processes. However, additional studies are required to determine the exact relationships between system geometry (aperture), flow mode, and the transition times between these regimes.

The studied setup can be expected to represent the extreme end member in terms of aperture dimension and consequently flow velocities of natural fractured systems. Fracture apertures studied in our work are less likely to appear in high numbers and also are at the far end of classical aperture distributions. However, they may substantially contribute to the formation of preferential pathways (e.g., in karst systems where additional solution has increased apertures). As such, they may play a vital role for example, in the context of percolation cluster studies [*Berkowitz and Adler*, 1998; *Adler et al.*, 2012].

Notation

$\boldsymbol{\alpha}$ color function particle state

$\boldsymbol{\alpha_k}$ kernel normalization constant

$\mathbf{a_i}$ particle acceleration

$\boldsymbol{A}$ interaction force kernel constant

$\boldsymbol{\beta}$ color function particle state

$\boldsymbol{B}$ interaction force kernel constant

$\boldsymbol{Bo}$ Bond number

$\boldsymbol{Ca}$ capillary number

$\boldsymbol{c_0}$ speed of sound

$\boldsymbol{c_i(\cdot)}$ particle color function

$\boldsymbol{\delta(\cdot)}$ Dirac delta function

$\boldsymbol{\delta_{\alpha,\beta}(\cdot)}$ Kronecker delta function for the color function evaluation

$\boldsymbol{\Delta d}$ bounce-back distance

$\boldsymbol{\hat{e}_{ij}}$ unit vector pointing from particle i to particle j

$\boldsymbol{\epsilon}$ equation of state constant

$\boldsymbol{F}$ force

$\boldsymbol{F_i^g}$ gravitational force acting on a particle

$\boldsymbol{F_{ij}^I}$ interaction force acting between two different particles

$\boldsymbol{F_{ij}^P}$ force due to a pressure gradient between two particles

$\boldsymbol{F_{ij}^V}$ viscous force acting between two particles

$\boldsymbol{g}$ gravitational acceleration

$\boldsymbol{\gamma}$ equation of state scaling coefficient

$\boldsymbol{h}$ kernel support range

i particle index

j particle index

m mass

μ viscosity

∇ nabla function

n number density

n_i^s state-specific number density for the color function

N number of particles

∇^2 Laplacian

Ω continuous domain

P pressure

P_0 background pressure

∂ partial derivative

ϕ proximity ratio for the bounce-back condition

ψ particle state for the surface normal calculation

q relative interparticle distance with respect to the kernel support range

r interparticle distance

ρ density

ρ_0 equilibrium reference density

σ surface tension

s_{ff} fluid-fluid particle interaction force strength

s_{sf} solid-fluid particle interaction force strength

$\hat{s}_i$ surface normal

t time

v velocity

$\bar{v}_i$ extrapolated velocity

ΔV particle volume

$W(\cdot)$ kernel function

$W_1(\cdot)$ interaction force kernel function

$W_2(\cdot)$ interaction force kernel function

x particle position

Δx equilibrium interparticle spacing

Acknowledgments

This work was funded by the Deutsche Forschungsgemeinschaft (DFG; German Research Foundation) under grant No. SA 501/26-1 and KO 53591/1-1. A.M. Tartakovsky was supported by the U.S. Department of Energy Office of Advanced Scientific Computing Research Program. M.D. acknowledges the funding from the European Research Council through the project MHetScale (Grant agreement No. 617511). The authors would like to thank C. Noubactep for providing laboratory equipment. All experimental data are available from the corresponding author upon request.

References

Adami, S., X. Y. Hu, and N. A. Adams (2012), A generalized wall boundary condition for smoothed particle hydrodynamics, *Journal of Computational Physics*, *231*, 7057–7075, doi:10.1016/j.jcp.2012.05.005.

Adler, P. M., J.-F. Thovert, and V. Mourzenko (2012), *Fractured Porous Media*, 184 pp., Oxford University Press, doi:10.1093/acprof:oso/9780199666515.001.0001.

Alava, M., M. Dubé, and M. Rost (2004), Imbibition in disordered media, *Advances in Physics*, *8732*(March 2015), 53, doi:10.1080/00018730410001687363.

Alder, B. J., and T. E. Wainwright (1959), Studies in Molecular Dynamics. I. General Method, *Journal of Chemical Physics*, *31*(2), 459, doi:10.1063/1.1730376.

Barenblatt, G. I., I. P. Zheltov, and I. N. Kochina (1960), Basic Concepts in the Theory of Seepage of Homogenous Liquids in Fissured Rocks Strata, *Journal of Applied Mathematics and Mechanics*, *24*, 1286–1303.

Batchelor, K. (2000), *An Introduction to Fluid Dynamics*, 658 pp., Cambridge University Press, London, doi:10.1017/CBO9780511800955.

Bell, J. M., and F. K. Cameron (1906), The flow of liquids through capillary spaces, *The Journal of Physical Chemistry*, *50*(30), 658–674, doi:10.1021/j150080a005.

Berkowitz, B., and P. M. Adler (1998), Stereological analysis of fracture network structure in geological formations, *Journal of Geophysical Research: Solid Earth*, *103*(B7), 15339–15360, doi:10.1029/98JB01072.

Bodvarsson, G. S., T. M. Bandurraga, and Y. S. Wu (1997), The Site-Scale Unsaturated Zone Model of Yucca Mountain, Nevada, for the Viability Assessment, *Tech. rep.*, Lawrence Berkeley National Laboratory, Berkeley.

Bouchaud, E. (1997), Scaling properties of cracks, *Journal of Physics: Condensed Matter*, *9*(21), 4319–4344, doi:10.1088/0953-8984/9/21/002.

Cleary, P. W. (1998), Modelling confined multi-material heat and mass flows using SPH, *Applied Mathematical Modelling*, *22*(12), 981–993, doi:10.1016/S0307-904X(98)10031-8.

Cummins, S. J., and M. Rudman (1999), An SPH Projection Method, *Journal of Computational Physics*, *152*(2), 584–607, doi:10.1006/jcph.1999.6246.

Dahan, O., R. Nativ, E. M. Adar, B. Berkowitz, and Z. Ronen (1999), Field observation of flow in a fracture intersecting unsaturated chalk, *Water Resources Research*, *35*(11), 3315–3326, doi:10.1029/1999WR900198.

Dahan, O., R. Nativ, M. Adar, B. Berkowitz, and N. Weisbrod (2000), On Fracture Structure and Preferential Flow in Unsaturated Chalk, *Ground Water*, *38*(3), 444–451.

de Gennes, P. (1985), Wetting: statics and dynamics, *Reviews of Modern Physics*, *57*(3), 827–863, doi:10.1103/RevModPhys.57.827.

Dehnen, W., and H. Aly (2012), Improving convergence in smoothed particle hydrodynamics simulations without pairing instability, *Monthly Notices of the Royal Astronomical Society*, *425*, 1068–1082, doi:10.1111/j.1365-2966.2012.21439.x.

Dershowitz, W. S., and H. H. Einstein (1988), Characterizing rock joint geometry with joint system models, *Rock Mechanics and Rock Engineering*, *21*(1), 21–51, doi:10.1007/BF01019674.

Dragila, M. I., and N. Weisbrod (2003), Parameters affecting maximum fluid transport in large aperture fractures, *Advances in Water Resources*, *26*, 1219–1228, doi:10.1016/j.advwatres.2003.09.002.

Dragila, M. I., and N. Weisbrod (2004), Fluid motion through an unsaturated fracture junction, *Water Resources Research*, *40*, 1–11, doi:10.1029/2003WR002588.

Faybishenko, B., S. M. Benson, and J. E. Gale (2015), *Dynamics of Fluids and Transport in Complex Fractured-Porous Systems*, John Wiley \& Sons, Ltd., Washington D.C., doi:10.1002/9781118877517.

Ganzenmüller, G., M. Steinhauser, and P. Van Liedekerke (2011), Implementation of SPH in LAMMPS, *Tech. rep.*

Ghezzehei, T. A. (2004), Constraints for flow regimes on smooth fracture surfaces, *Water Resources Research*, *40*, 1–14, doi:10.1029/ 2004WR003164.

912 Glass, R. J., and R. a. LaViolette (2004), Self-organized spatial-temporal structure within
913 the fractured Vadose Zone: Influence of fracture intersections, *Geophysical Research*
914 *Letters*, *31*, 1–4, doi:10.1029/2004GL019511.
915 Glass, R. J., M. J. Nicholl, H. Rajaram, and T. R. Wood (2003), Unsaturated flow
916 through fracture networks: Evolution of liquid phase structure, dynamics, and the
917 critical importance of fracture intersections, *Water Resources Research*, *39*(12), doi:
918 10.1029/2003WR002015.
919 Guarracino, L. (2006), A fractal constitutive model for unsaturated flow in fractured hard
920 rocks, *Journal of Hydrology*, *324*(1-4), 154–162, doi:10.1016/j.jhydrol.2005.10.004.
921 Gunn, J. (1981), Hydrological processes in karst depressions, *Zeitschrift Für Geomor-*
922 *phologie*, *25*(3), 313–331.
923 Harris, J. W., and H. Stocker (1999), Handbook of mathematics and computational sci-
924 ence, *Computers \& Mathematics with Applications*, *37*(3), 133, doi:10.1016/S0898-
925 1221(99)90385-1.
926 Hasseine, A., A. Bellagoun, and H.-J. Bart (2011), Analytical solution of the droplet
927 breakup equation by the Adomian decomposition method, *Applied Mathematics and*
928 *Computation*, *218*(5), 2249–2258, doi:10.1016/j.amc.2011.07.041.
929 Holmes, D., J. Williams, and P. Tilke (2011), Smooth particle hydrodynamics simulations
930 of low Reynolds number flows through porous media, *International Journal for Numeri-*
931 *cal and Analytical Methods in Geomechanics*, *35*, 419–437, doi:10.1002/nag.898.
932 Hoogerbrugge, P., and J. Koelman (1992), Simulating microscopic hydrodynamic phe-
933 nomena with dissipative particle dynamics, *Europhys. Lett.*, *19*(June), 155–160, doi:
934 10.1209/0295-5075/19/3/001.
935 Hu, X. Y., and N. A. Adams (2007), An incompressible multi-phase SPH method, *Journal*
936 *of Computational Physics*, *227*(1), 264–278, doi:10.1016/j.jcp.2007.07.013.
937 Huang, H., P. Meakin, and M. Liu (2005), Computer simulation of two-phase immiscible
938 fluid motion in unsaturated complex fractures using a volume of fluid method, *Water*
939 *Resources Research*, *41*, 1–12, doi:10.1029/2005WR004204.
940 Ji, S.-h., M. J. Nicholl, R. J. Glass, and K.-k. Lee (2004), Influence of a simple fracture
941 intersection on density-driven immiscible flow : Wetting vs . nonwetting flows, *Geo-*
942 *physical Research Letters*, *31*(June), 10–13, doi:10.1029/2004GL020045.
943 Ji, S.-H., M. J. Nicholl, R. J. Glass, and K.-K. Lee (2006), Influence of simple fracture
944 intersections with differing aperture on density-driven immiscible flow: Wetting versus

945 nonwetting flows, *Water Resources Research*, *42*, 1–10, doi:10.1029/2006WR004953.
946 Kordilla, J., A. Tartakovsky, and T. Geyer (2013), A Smoothed Particle Hydrodynamics
947 model for droplet and film flow on smooth and rough fracture surfaces, *Advances in*
948 *Water Resources*, *59*, 1–14, doi:10.1016/j.advwatres.2013.04.009.
949 LaViolette, R. A. (2003), Convergent flow observed in a laboratory-scale unsaturated frac-
950 ture system, *Geophysical Research Letters*, *30*(2), 10–12, doi:10.1029/2002GL015775.
951 Libersky, L. D., A. G. Petschek, T. C. Carney, J. R. Hipp, and F. A. Allahdadi (1993),
952 High Strain Lagrangian Hydrodynamics, doi:10.1006/jcph.1993.1199.
953 Liu, G. R., and M. Liu (2000), *Smoothed Particle Hydrodynamics. A Meshfree Particle*
954 *Method*, 449 pp., World Scientific, Singapore.
955 Liu, H. H., R. Salve, J. S. Wang, G. S. Bodvarsson, and D. Hudson (2004), Field investi-
956 gation into unsaturated flow and transport in a fault: Model analyses, *Journal of Con-*
957 *taminant Hydrology*, *74*(1-4), 39–59, doi:10.1016/j.jconhyd.2004.02.004.
958 Liu, M., P. Meakin, and H. Huang (2007), Dissipative particle dynamics simulation of
959 fluid motion through an unsaturated fracture and fracture junction, *Journal of Computa-*
960 *tional Physics*, *222*, 110–130, doi:10.1016/j.jcp.2006.07.017.
961 Liu, M. B., and G. R. Liu (2010), Smoothed Particle Hydrodynamics (SPH): an Overview
962 and Recent Developments, *Archives of Computational Methods in Engineering*, *17*(1),
963 25–76, doi:10.1007/s11831-010-9040-7.
964 Monaghan, J. J. (1982), Why particle methods work, *SIAM: SIAM Journal on Scientific*
965 *Computing*, *3*(4), 422–433, doi:10.1137/0903027.
966 Monaghan, J. J. (1992), Smoothed particle hydrodynamics, *Reports on Progress in Physics*,
967 *68*, 1703–1759, doi:10.1088/0034-4885/68/8/R01.
968 Monaghan, J. J. (2005), Smoothed particle hydrodynamics, *Reports on Progress in Physics*,
969 *68*(8), 1703–1759, doi:10.1088/0034-4885/68/8/R01.
970 Morris, J. P., P. J. Fox, and Y. Zhu (1997), Modeling Low Reynolds Number Incom-
971 pressible Flows Using SPH, *Journal of Computational Physics*, *136*(1), 214–226, doi:
972 10.1006/jcph.1997.5776.
973 Nicholl, M. J., and R. J. Glass (2005), Infiltration into an Analog Fracture, *Vadose Zone*
974 *Journal*, *4*(4), 1123, doi:10.2136/vzj2004.0110.
975 Nimmo, J. R. (2012), Preferential flow occurs in unsaturated conditions, *Hydrological Pro-*
976 *cesses*, *26*(5), 786–789, doi:10.1002/hyp.8380.

977 Or, D. (2008), Scaling of capillary, gravity and viscous forces affecting flow morphol-
978 ogy in unsaturated porous media, *Advances in Water Resources*, *31*(9), 1129–1136, doi:
979 10.1016/j.advwatres.2007.10.004.
980 Or, D., and T. A. Ghezzehei (2000), Dripping into subterranean cavities from unsaturated
981 fractures under evaporative conditions, *Water Resources Research*, *36*(2), 381–393, doi:
982 10.1029/1999WR900311.
983 Plimpton, S. (1995), Fast parallel algorithms for short-range molecular dynamics, *Journal*
984 *of Computational Physics*, *117*(1), 1–19.
985 Plimpton, S., P. Crozier, and A. Thompson (2007), LAMMPS-large-scale atomic/molecular
986 massively parallel simulator, *Sandia National Laboratories*, *18*.
987 Podgorski, T., J.-M. Flesselles, and L. Limat (2001), Corners, Cusps, and
988 Pearls in Running Drops, *Physical Review Letters*, *87*(3), 036102, doi:
989 10.1103/PhysRevLett.87.036102.
990 Ponson, L., D. Bonamy, and E. Bouchaud (2006), Two-Dimensional Scaling Proper-
991 ties of Experimental Fracture Surfaces, *Physical Review Letters*, *96*(3), 035506, doi:
992 10.1103/PhysRevLett.96.035506.
993 Sigalotti, L. D. G., J. Daza, and A. Donoso (2006), Modelling free surface flows with
994 smoothed particle hydrodynamics, *Condensed Matter Physics*, *9*(2), 359–366.
995 Sobolev, V. D., N. V. Churaev, M. G. Velarde, and Z. M. Zorin (2000), Surface Tension
996 and Dynamic Contact Angle of Water in Thin Quartz Capillaries, *Journal of Colloid*
997 *and Interface Science*, *222*(1), 51–54, doi:10.1006/jcis.1999.6597.
998 Su, G. W., J. T. Geller, K. Pruess, and F. Wen (1999), Experimental studies of water seep-
999 age and intermittent flow in unsaturated, rough-walled fractures, *Water Resources Re-*
1000 *search*, *35*(4), 1019, doi:10.1029/1998WR900127.
1001 Su, G. W., J. T. Geller, K. Pruess, and J. R. Hunt (2001), Solute transport along preferen-
1002 tial flow paths in unsaturated fractures, *Water Resources Research*, *37*(10), 2481–2491,
1003 doi:10.1029/2000WR000093.
1004 Tartakovsky, A., and P. Meakin (2005a), Modeling of surface tension and contact an-
1005 gles with smoothed particle hydrodynamics, *Physical Review E*, *72*, 026301, doi:
1006 10.1103/PhysRevE.72.026301.
1007 Tartakovsky, A., and P. Meakin (2005b), Simulation of Unsaturated Flow in Complex
1008 Fractures Using Smoothed Particle Hydrodynamics, *Vadose Zone Journal*, *4*(3), 848–
1009 855, doi:10.2136/vzj2004.0178.

1010 Tartakovsky, A., and P. Meakin (2006), Pore scale modeling of immiscible and miscible fluid flows using smoothed particle hydrodynamics, *Advances in Water Resources*, *29*(10), 1464–1478, doi:10.1016/j.advwatres.2005.11.014.

1013 Tartakovsky, A., and A. Panchenko (2016), Pairwise Force Smoothed Particle Hydrodynamics model for multiphase flow: Surface tension and contact line dynamics, *Journal of Computational Physics*, *305*, 1119–1146, doi:10.1016/j.jcp.2015.08.037.

1016 Tartakovsky, A., K. F. Ferris, and P. Meakin (2009), Lagrangian particle model for multiphase flows, *Computer Physics Communications*, *180*(10), 1874–1881, doi:10.1016/j.cpc.2009.06.002.

1019 Tartakovsky, A., N. Trask, K. Pan, B. Jones, W. Pan, and J. R. Williams (2016), Smoothed particle hydrodynamics and its applications for multiphase flow and reactive transport in porous media, *Computational Geosciences*, *20*(4), 807–834, doi:10.1007/s10596-015-9468-9.

1023 Tokunaga, T. K., and J. Wan (1997), Water film flow along fracture surfaces of porous rock, *Water Resources Research*, *33*(6), 1287, doi:10.1029/97WR00473.

1025 Tokunaga, T. K., and J. Wan (2001), Surface-zone flow along unsaturated rock fractures, *Water Resources Research*, *37*(2), 287, doi:10.1029/2000WR900242.

1027 Tokunaga, T. K., K. R. Olson, and J. Wan (2005), Infiltration flux distributions in unsaturated rock deposits and their potential implications for fractured rock formations, *Geophysical Research Letters*, *32*(5), 1–4, doi:10.1029/2004GL022203.

1030 Trinchero, P., R. Beckie, X. Sanchez-Vila, and C. Nichol (2011), Assessing preferential flow through an unsaturated waste rock pile using spectral analysis, *Water Resources Research*, *47*(7), 1–11, doi:10.1029/2010WR010163.

1033 Wang, Z.-B., R. Chen, H. Wang, Q. Liao, X. Zhu, and S.-Z. Li (2016), An overview of smoothed particle hydrodynamics for simulating multiphase flow, *Applied Mathematical Modelling*, *40*(23-24), 9625–9655, doi:10.1016/j.apm.2016.06.030.

1036 Washburn, E. W. (1921), The dynamics of capillary flow, *Physical Review*, *17*, 273–283, doi:10.1103/PhysRev.17.273.

1038 Watkins, S., A. Bhattal, N. Francis, J. Turner, and A. Whitworth (1996), A new prescription for viscosity in Smoothed Particle Hydrodynamics, *Astronomy and Astrophysics Supplement Series*, *119*, 177–187.

1041 Wendland, H. (1995), Piecewise polynomial, positive definite and compactly supported radial functions of minimal degree, *Advances in computational Mathematics*, *4*(1), 389–

396.

Williams, P. W. (2008), The role of the epikarst in karst and cave hydrogeology: A review, *International Journal of Speleology*, *37*(1), 1–10, doi:10.5038/1827-806X.37.1.1.

Wood, T. R., and H. Huang (2015), Experimental and modeling studies of episodic air-water two-phase flow in fractures and fracture networks, in *Fluid Dynamics in Complex Fractured-Porous Systems*, p. 209, John Wiley \& Sons, Ltd.

Wood, T. R., M. J. Nicholl, and R. J. Glass (2002), Fracture intersections as integrators for unsaturated flow, *Geophysical Research Letters*, *29*(24), 2191, doi: 10.1029/2002GL015551.

Wood, T. R., M. J. Nicholl, and R. J. Glass (2005), Influence of fracture intersections under unsaturated , low-flow conditions, *Water Resources Research*, *41*, W04017, doi: 10.1029/2004WR003281.

Zhu, Y. I., P. J. Fox, and J. P. Morris (1999), A pore-scale numerical model for flow through porous media, *International Journal for Numerical and Analytical Methods in Geomechanics*, *23*, 881–904.